CHALMERS
UNIVERSITY OF TECHNOLOGY

Multi-purpose parameter development for high productivity in Laser Powder Bed Fusion of IN718

Master’s thesis in Materials Engineering (MPAEM)

NEGAR PANAHI

Department of Industrial and Materials Science
CHALMERS UNIVERSITY OF TECHNOLOGY
Gothenburg, Sweden 2020

Master's thesis 2020

Multi-purpose parameter development for high productivity in Laser Powder Bed Fusion of IN718

NEGAR PANAHI

Department of Industrial and Materials Science
Division of Materials and Manufacturing
Chalmers University of Technology
Gothenburg, Sweden 2020

Multi-purpose parameter development for high productivity in Laser Powder Bed Fusion of IN718
NEGAR PANAHI

Supervisor: Zhuoer Chen, Post doc at Chalmers University of Technology
Examiner: Eduard Hryha, Professor at Chalmers University of Technology

Master's Thesis 2020
Department of Industrial and Materials Science
Division of Materials and Manufacturing
Chalmers University of Technology
SE-412 96 Gothenburg
Telephone +46 31 772 1000

Cover: Spherical pores in the microstructure of IN718 manufactured through Laser Powder Bed Fusion method.

Typeset in LaTeX
Printed by Chalmers Reproservice
Gothenburg, Sweden 2020

Multi-purpose parameter development for high productivity in Laser Powder Bed Fusion of IN718
NEGAR PANAHI
Department of Industrial and Materials Science
Chalmers University of Technology

Abstract

Laser-Powder Bed Fusion (L-PBF) is one of the main metal Additive Manufacturing (AM) technologies that has seen major developments in terms of materials development, applications, design and quality assurance, etc. One of the main limitations of L-PBF process is the high cost of machine time dedicated to the production of the parts. It is therefore desirable to speed up the process, making wide application of the process more economically viable. In this thesis, we aim to increase the productivity of L-PBF processing of IN718 by using a layer thickness (80 μm) which is at least two times larger than the state-of-art (20 - 40 μm). An increase in the layer thickness essentially decreases the amount of energy input by the laser beam to the material per unit volume. Consequently, other process parameters including but not limited to laser power, hatch distance, scanning speed, etc., shall be adjusted accordingly to enable full densification of the part. Additionally, other aspects of the product qualities should be considered during the optimization process, which includes surface finish, geometrical compliance, and microstructure.

This thesis employs statistical Design of Experiments (DoE) and regression analysis for the optimization of key L-PBF processing parameters. In the meantime, two separate experimental campaigns were conducted using similar DOE matrix (central composite design) but different sample geometries. In the first experimental campaign, a simple cubic specimen was used, a processing window with optimized combination of laser power, scan speed, hatch distance was determined using regression analysis based on the measurements of relative densities from cross-sections. In the second experimental campaign, more complex designs (staircase geometry) were used to characterize the influence of heat accumulation effects at thin wall structures on relative density and surface roughness. The applicabilities of volumetric energy density (VED) and its normalised form for evaluation of process stability are discussed.

Keywords: Additive manufacturing, Laser powder bed fusion, Porosity, Powder layer thickness, IN718, Scanning speed, Laser power, Hatch distance, Image analysis, Surface roughness

Acknowledgements

I would like to express my sincere gratitude to my supervisor Dr. Zhuoer Chen for his continuous support during this journey as well as Prof. Eduard Hryha for his valuable guidance and comments.
I also wish to thank IMS staff for their kind support during the experimental phase of this project.

Negar Panahi, Gothenburg, September 2020

Contents

List of Figures xi

List of Tables xiii

1 Introduction 1
- 1.1 Overview of metal additive manufacturing . . . 1
- 1.2 Metal Additive Manufacturing techniques . . . 1
- 1.3 Laser Powder Bed Fusion (L-PBF) . . . 3
- 1.4 IN718 in L-PBF . . . 4
- 1.5 L-PBF quality control . . . 4
  - 1.5.1 Porosity . . . 5
  - 1.5.2 Microstructure . . . 6
  - 1.5.3 Surface roughness . . . 7
- 1.6 Defect generation in L-PBF . . . 7
- 1.7 Process development . . . 7
  - 1.7.1 Volumetric Energy Density (VED) . . . 8
  - 1.7.2 Dimensionless energy per unite volume (E^*) . . . 8
- 1.8 Study objectives . . . 9

2 Experimental methods 11
- 2.1 Material and L-PBF machine . . . 11
- 2.2 Design of Experiment . . . 11
  - 2.2.1 Central Composite Design . . . 12
  - 2.2.2 Sample geometry . . . 14
- 2.3 Analysis . . . 16
  - 2.3.1 Image Analysis . . . 16
  - 2.3.2 Regression Analysis . . . 18

3 Results and discussion 19
- 3.1 Porosity measurement . . . 19
  - 3.1.1 C-series . . . 19
  - 3.1.2 T-series . . . 22
- 3.2 Surface roughness . . . 26
- 3.3 Regression analysis of the results . . . 28
  - 3.3.1 R-Studio Model . . . 28
  - 3.3.2 JMP Model . . . 30
- 3.4 Process development . . . 30

3.4.1 Volumetric Energy Density 30
3.4.2 Dimensionless energy per unite volume 32

4 Conclusions **35**

Bibliography **37**

A Appendix 1 **I**
A.1 Detailed result of T-series II
A.2 R-studio VIII
A.2.1 C-series VIII
A.2.2 T-series IX
A.3 Dimensionless energy per unite volume XI

List of Figures

1.1 Schematic drawing of L-PBF process 3

2.1 Schematic drawing of the performed cuts on C-series 15
2.2 T-series samples' geometry - dimensions are in millimeter 15
2.3 Section designation of T-series based on the printed thickness 17
2.4 Schematic explanation of Rq and Rt 17

3.1 Optical images taken from C-series 20
3.2 Optical images from etched C-series samples 21
3.3 Optical images from T-series samples 23
3.4 Optical images from etched T-series samples 24
3.5 Geometrical effect on the porosity in T-series 25
3.6 Correlation between surface roughness and the applied VED in T-series 26
3.7 Pareto plot for C-series model 29
3.8 Pareto plot for T-series model 29
3.9 Density vs. VED 31
3.10 Contour plot from JMP software based on dimensionless parameters in C-series 33
3.11 Contour plot from JMP software based on dimensionless parameters in T-series 33

List of Tables

1.1 Comparison between L-PBF, EBM and DED 3

2.1 Chemical composition of the IN718 powder 11
2.2 High and low levels of process parameters 12
2.3 Parameters variation among C-series samples 13
2.4 Experimental runs, T-series 14
2.5 Grinding and polishing steps applied on the samples 16

3.1 Porosity results of C-series 19
3.2 Porosity results of T-series 22
3.3 Surface roughness results of T-series in section 1 of each horizontal and vertical plane 27
3.4 Process parameters used in equations 1.2-1.4 32

A.1 Detailed results of T-series; samples T-1 to T-4 II
A.2 Detailed results of T-series; samples T-5 to T-9 III
A.3 Detailed results of T-series; samples T-10 to T-14 IV
A.4 Detailed results of T-series; samples T-15 to T-19 V
A.5 Detailed results of T-series; samples T-20 to T-24 VI
A.6 Detailed results of T-series; samples T-25 to T-28 VII
A.7 Dimensionless parameters based on in equations 1.2-1.4 for C-series . XI
A.8 Dimensionless parameters based on in equations 1.2-1.4 for T-series . XII

1

Introduction

1.1 Overview of metal additive manufacturing

Additive Manufacturing (AM) or 3D printing is a method of manufacturing components by joining materials according to a 3D computer-aided design (CAD), usually in a layer by layer fashion [1,2]. AM can be considered as an improved version of rapid prototyping which has previously been used only for producing prototypes or porous components. The application of AM products has increased due to the technology advancement in AM equipment and process control [3].

AM is the generalized term for many different processes: material jetting, material extrusion, binder jetting, vat photo-polymerization, powder bed fusion, sheet lamination and directed energy deposition [1]. The various AM processes differ in feedstock material (powder, wire, liquid, sheets and so on), the volume capacity, the material which can be used, material deposition rate, quality and resolution of the final product, required post treatment, etc. In general, AM has the benefits of shortened lead time, lower buy-to-fly ratio and capability of manufacturing highly customized, complex-shaped components whereas conventional subtractive methods incur cost and time for tooling, fixturing and post machining [1,4].

Since additive manufactured parts are directly produced in near-net shapes, less machining as post treatment is required to achieve desired final dimensions which may lead to lower manufacturing costs in total [5]. However, for each case of production, the rationality of AM application shall be evaluated based on the volume of the production, part's complexity and level of customization. AM methods are more favored when the level of complexity and customization are high [1]. Furthermore, in order to achieve high quality in AM components, usually a slow pace of production shall be applied. AM is currently limited to the production of high-value components in relatively small production volumes for niche markets [1,6].

1.2 Metal Additive Manufacturing techniques

Metal AM can be divided into three main categories based on the form of feedstock material and deposition methods: powder bed systems, powder feeding systems, and wire feed systems [7]. The energy source required for the production can be provided by laser, arc or electron beam [7]. Main metal AM techniques include:

- Laser Powder Bed Fusion (L-PBF)
- Electron Beam Melting (EBM)
- Directed Energy Deposition (DED)

The L-PBF process can be viewed as many iterations of two steps: deposition/spreading of a thin layer of metallic powder on the building platform and laser scanning at the selected areas designated by the sliced CAD profile, which results in melting and consolidation of metal powders [4]. Upon finishing of the laser scan over the powder bed surface, the building platform is dropped by a certain amount equivalent to the pre-defined layer thickness and the next iteration starts. The L-PBF process is conducted in a closed chamber flooded with inert protection gas (e.g., argon, nitrogen) while the oxygen level in the processing chamber is closely monitored.

Although EBM uses powder bed as well, it is a very different process compared to L-PBF. EBM uses electron beam as the heating sources and therefore requires a vacuum process chamber. Moreover, prior to the melting step, a pre-sintering step is required in EBM [8]. The pre-sintered powder bed act as a support structure to some extent whereas supports should be in place for structures such as overhangs in L-PBF parts by design. The support structure performs two functions, firstly restrict thermal distortion and secondly conduct heat away from overhanging solid [8]. As a general design rule, for the same geometry EBM parts usually requires less support compared to L-PBF parts due to the fact that EBM is conducted at rather high temperatures (400-1000 °C) while L-PBF is typically conducted with the build plate heated up to 80 - 200 °C, therefore the residual stress during EBM process is much lower than that in L-PBF [8]. Multiple parts can be stacked on top of one another in EBM machine to make full use of the process chamber while this is usually not possible for L-PBF process. On the other hand, it takes longer for the build chamber to cool down after the build job is finished in EBM. In addition, the pre-sintered powder that were recycled from an EBM build job needs to be broken apart for the next use. The powder size and powder layer thickness are larger in EBM compared to L-PBF, which leads to a higher surface roughness [8].

In DED methods, the energy source is directed towards the same spot where the feedstock material is fed to, leading to the formation of a melt pool [8]. DED uses either wire or powder as the feedstock and the energy source can be arc, laser or electron beam [8]. DED method can be considered as similar to the welding process when using arc as heat source and wire as feedstock. DED is capable of producing large components in contrast to EBM and L-PBF [8]. According to ASTM standard, due to the similarity to the welding process, DED can also be used as a repair method [9]. A summary of the comparison between L-PBF, EBM, and DED methods can be found in table 1.1.

Table 1.1: Comparison between L-PBF, EBM and DED

	L-PBF	**EBM**	**DED**
Energy source	Laser	Electron beam	Laser, arc, etc.
Feedstock	Powder	Powder	Wire or Powder
Support structure	Required	Required less	Required
Powder size	10–45 μm	45–106 μm	20–200 μm
Chamber atmosphere	Inert gas	Vacuum	Shield gas steam
Residual stress	++	+	++
Resolution	++	+	+

1.3 Laser Powder Bed Fusion (L-PBF)

A schematic drawing of L-PBF process is illustrated in figure 1.1. During L-PBF process, the laser energy is adjusted to achieve a certain depth of melt pool so that the previously melted and solidified metal are remelted along with the newly deposited layer for sound metallurgical bonding between layers [4]. However, the amount of this energy penetration through previous layers is critical, too high energy penetrations may result in keyholes creation, whereas too low energy penetration may lead to lack of fusion [10]. Keyhole formation together with destabilized melt pool and increased amount of gas bubbles locked in the structure, lead to increased amount of porosity in the final product [11]. Furthermore, it is not energy efficient to induce high energy penetrations [11].

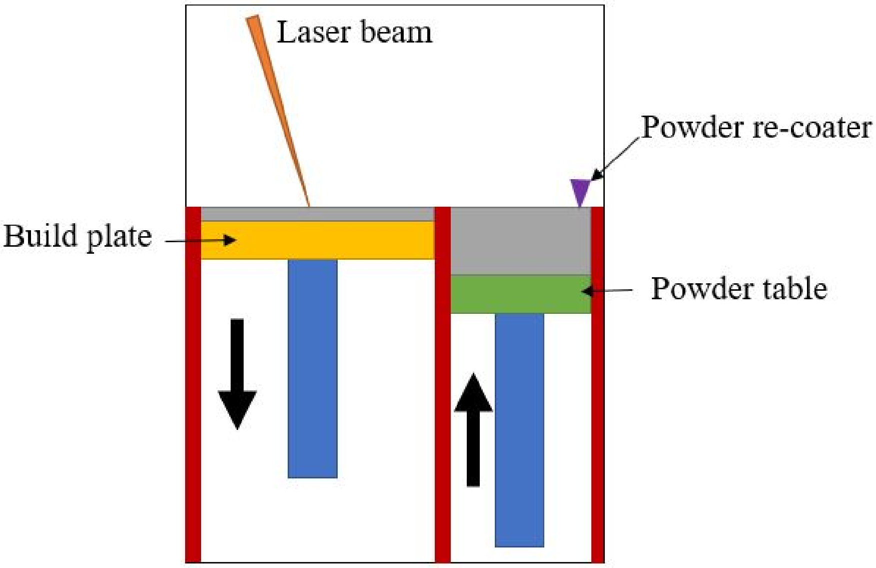

Figure 1.1: Schematic drawing of L-PBF process

The L-PBF advantage is to reduce the time needed for the production since it introduces a faster production [11]. One advantage of the L-PBF process is its low buy-to-fly ratio (the ratio between the weight of the purchased raw material and the weight of the final product), since the feedstock powder can be recycled. Although L-PBF provides better resolution in comparison to EBM and DED, L-PBF products still may need to undergo polishing, surface hardening, and stress relieving as post treatments [11].

1.4 IN718 in L-PBF

For critical applications such as aerospace and nuclear components that require excellent mechanical properties at high temperatures, superalloys can be used as an alternative to conventional materials such as stainless steels [4]. While keeping the outstanding resistance to fatigue and corrosion, IN718 can maintain its mechanical properties at high temperatures [4]. Furthermore, Nickel-based superalloys show a high creep and oxidation resistance [12].

In addition, IN718 is already used as the material for turbine blades and combustion chambers [12]. Components can be made from IN718 using different methods such as casting, forging and powder metallurgy [12]. However, due to the high strength, low thermal conductivity and high hardness of IN718, when producing through subtractive methods, the machining devices will be subjected to high levels of wear [4,13]. That is the reason why additive manufacturing of IN718 with less required post machining, is a subject of interest [4]. However, due to the complex thermal history of additive manufactured IN718, different kinds of defects may be activated, which deteriorates mechanical properties [13]. In addition, the manufacturing cost of L-PBF IN718 parts incurred from raw material, AM machine maintenance, energy consumption and post-machining serve as a crucial hurdle for wider adoption of the technology for producing IN718 parts.

1.5 L-PBF quality control

Although the applicability of AM methods has been proved for some metallic materials such as Ti-6Al-4V and nickel-based superalloys, the field yet has much more to investigate [2]. The main challenge in AM can be defined as how to reach proper density, microstructure, and mechanical properties together with sound confidence in quality control of the component [2]. Various types of defects including lack-of-fusion and gas pores may contribute to the lower dynamic properties of a L-PBF produced component [14]. These abnormalities can act as a stress intensifier that leads to premature failure of the components. This issue may be prevented through optimization of key processing parameters of L-PBF process [2].

The L-PBF process involves a cyclic heating and cooling and results in spatially variable thermal history in a part of geometrical complexity, and consequently results in inhomogeniety in the material such as compositional variation [5]. Moreover, the rapid solidification and directional cooling during the L-PBF introduce highly

non-equilibrium microstructure that is often anisotropic with respect to the build direction [15].
The variability in microstructure and composition might be critical for the performance of the products [5].

Quality control of L-PBF manufactured component concerns different aspects such as porosity, microstructure, residual stress, homogeneity, texture, surface roughness, etc. Depending on the expected function of the component, each subject may be considered as a priority to look into. In this study, the focus would be on the porosity level and distribution. In addition, the surface roughness of the components will be characterized as secondary measures of the quality.

1.5.1 Porosity

In general, porosities can act as a stress concentration areas and affect the mechanical properties of a component severely. For instance, the presence of pores may result in a lower fatigue and creep resistance of the AM produced IN718 [17,18].

The porosity level of L-PBF parts is affected by and/or can be correlated to the applied process parameters in the production [11]. The energy input in each layer by the laser beam and its interaction with the powder bed determine the quality of the parts[11]. In other words, the level of the porosity is dependent on the powder size, shape and distribution, scanning strategies including scanning speed, laser power, hatch distance, powder layer thickness, and so on [18]. For instance, as described in [18], higher scanning speeds can result in a more irregular shape of pores and higher porosity in general.

In addition, by increasing laser power higher densities may be obtained [18], but as evaluated in [11], too high laser power may cause extra turbulence in the melt pool and increasing the porosity accordingly. The porosity found in the L-PBF produced IN718 microstructure, can be either spherically shaped and located inside the melt pools or irregularly shaped due to the lack of fusion and located at the boundaries between neighbouring layers and scan tracks, etc [4]. The spherical pores may result from the entrapped gas due to turbulent melt flow and entrapped gas or the gas pores pre-existing in the feedstock powders [4]. The gas pores can not be completely removed by post-treatments such as Hot Isostatic Pressure (HIP) [4].

The porosity of a component can be measured using different methods of density measurements including but not limited to Archimedes method, image analysis and X-Ray computed tomography [18]. Based on [18], the Archimedes method is very accurate but the image analyses can show almost the same results when for low porosity levels. One of the drawbacks of the image analysis method is its dependence on the resolution of the image and size, shape and distribution of the pores [18].

1.5.2 Microstructure

The strengthening mechanisms of IN718 include the solid solution strengthening and precipitation hardening, and the obtained microstructure is sensitive to the manufacturing process [12]. L-PBF process leads to a complex phase transformations resulting a specific columnar dendrites microstructure [20,21].

IN718 may contain different phases playing different roles [4]:

- γ $(Ni-Cr-Fe)$: The solid solution matrix of IN718 with face-centered cubic crystal structure [12].

- γ' $(Ni_3(Ti, Al, Nb))$: Hardening phase with its precipitation controllable by tailored heat treatment. This phase has a typical size of around 20 nm. γ' has a face-centered cubic crystal structure [12].

- γ'' (Ni_3Nb): Hardening phase with its precipitation controlled by tailored heat treatment. This phase has a typical size of 50-100 nm. γ'' has a a body-centered tetragonal crystal structure [21].

- δ (Ni_3Nb): Needle shaped precipitates located in the grain boundaries. Growth of δ phase consumes the Nb needed for the formation of desired γ''. However, rather low amounts of δ improve the creep resistance of the material by hindering the grain boundaries' movements. δ is ordered in an orthorhombic structure [12].

- *MC Carbides*: Precipitates inside the grains and at the grain boundaries in the shape of blocks. Similar to the δ phase low amounts and proper shapes of them can improve some mechanical properties. Also, when MC carbides exist inside the grains, by hindering dislocations' movements, they contribute to the increase of the strength [22].

Considering L-PBF as a non-equilibrium process, the IN718 part produced with L-PBF may show a columnar microstructure which is parallel to the building direction [4]. This dendritic and columnar microstructure happens due to the cooling rates as high as 10^5 °C/s in the process [4]. Furthermore, the final blank component may show a high amount of porosity which will affect the mechanical properties in case post-treatment is not applied on the component prior to the application [4]. In addition, the surface roughness of a blank part could be high enough to affect and weaken the mechanical properties [4].

It has been suggested that the higher VED is, the longer dendrites may be formed and stiffer structure may be obtained due to the stronger bonds between the dendrites [12].
The post-treatments such as heat treatments may guarantee the disappearance of the dendritic structure and also the formation of the phases such as γ' and γ'' which contribute to the hardening of the final product [4].

1.5.3 Surface roughness

Due to the layer-by-layer melting and solidification, L-PBF procedure is associated with the staircase and balling effect, leading to surface roughness of as-built component [23]. Surface roughness is an important property affecting the fatigue resistance of a component [3]. The advantage of using AM method in IN718 production is less required machining as post treatment. Thus, it is important to set the process parameters in a way resulting in the least possible surface roughness.

The effect of applying finer powders and smaller powder layer thickness has been proven to result in a lower surface roughness in L-PBF of Ti-64 [24]. In addition, the resulted surface finish of L-PBF Ti-64 has been reported to be three times better than an EBM produced one [24].

1.6 Defect generation in L-PBF

Various kinds of physical phenomena take place in L-PBF process leading to dynamical melt flow and defect formation [26,27]:

- **Balling effect**: Tendency of a liquid to minimize the surface tension by forming droplets.
- **Marangoni effect**: Temperature gradient and dependency of surface tension on the temperature results in surface tension gradient. Due to the high surface tension gradients in the melt pool, the melt penetrates through the depth of the specimen resulting in re-circulation of the melt flow. Re-circulation causes the melt spattering from the surface.
- **Recoil pressure**: Below the scanning spot, the temperature can be as high as boiling temperature leading to depression of the melt pool surface.

Combination of recoil pressure and Marangoni effect results in increased depth of melt pool [25].

1.7 Process development

L-PBF is highly sensitive to parameter variation [11]. Based on the following order, laser power density, powder layer thickness, and scanning speed together with powder particle size are parameters in L-PBF that are most effective on properties of the final product [11]. The scanning speed and laser power can be assumed to play the most important roles in the surface finish, porosity and the final mechanical properties of the L-PBF part [4]. In addition, the combination of laser power, hatch distance and scanning speed will define the properties and quality of the L-PBF part [4].

L-PBF products show a wide range of mechanical properties based on the parameters used in the production [11]. For example, the combination of low scanning speed and high laser power density in L-PBF increases the probability of keyholes formation, and when having high scanning speed and high laser power density, melt pools will be more unstable [27]. Considering the fact that each scan causes heat penetration towards already scanned layers, the amount of this heat penetration is dependent on the energy density of the laser [11]. The heat penetration can be measured by the depth of the melt pool and a process shall be evaluated as an optimal process if this depth of re-melted powder is close to the powder layer thickness [11].

By defining tracks as primary units the combination of them provides a layer in the L-PBF product [11], a track's height can be defined based on the powder layer thickness [11]. In addition, track's stability and continuity can be defined as a function of parameters: power density, powder layer thickness, scanning speed, and distribution of powder particle size [11].

Different kinds of approaches may be used to predict the expected quality of the component. In this study, the Volumetric Energy Density (VED) and Dimensionless energy per unite volume (E^*) have been used to map the results.

1.7.1 Volumetric Energy Density (VED)

Volumetric Energy Density with the unit of $[J/mm^3]$ and as described in equation 1.1, is claimed to be useful in studying the influence of four following parameters on the final characteristics of the final product: Laser Power (P) in Watt, Powder layer thickness (d) in μm, Hatch distance (H) in mm and Scanning speed (S) in mm/s [4].

VED is expected to express the level of fusion during the process [4]. Low fusion can be the result of a too low VED and vise versa [4]. It has also been claimed that an increase in the VED may result in lower porosity in general [4]. According to [4], various samples having different VED may show similar microstructures after post-treatments. According to [28], a decrease in VED can result in the lack of fusion. However, if the VED is too high, it can lead to keyholes formation.

$$VED = \frac{P}{S.H.d} \times 10^3 \tag{1.1}$$

1.7.2 Dimensionless energy per unite volume (E*)

Dimensionless energy per unite volume or normalized energy density has been defined to predict the final quality of the product based on its location in the designed map [2]. The map is built using $1/H^*$ on the y-axis and E^* on the x-axis. The final map can be constructed based on laser power P, scanning speed S, beam radius r_B, hatch distance H, and layer thickness d. Equations 1.2-1.3 show how E^* can be calculated [2]. In equations 1.2 and 1.3, the sign '*' denotes the dimensionless parameters which are defined as $d^* = 2d/r_B$, $H^* = H/r_B$ and $S^* = Sr_B/\alpha$. The absorptivity is represented by A. α and λ stand for thermal diffusivity and conductivity, respectively. Also, material related parameters such as density ρ, specific heat capacity C_p, melting temperature T_m and powder bed temperature T_0, have been taken to account [2].

$$P^* = AP/[r_B\lambda(T_m - T_0)] \quad (1.2)$$

$$E^* = P^*/S^*d^* = [AP/(2Sdr_B)][1/\rho C_p(T_m - T_0)] \quad (1.3)$$

In addition, normalized equivalent energy density E_0^*, is defined as described in the equation 1.4 [2]. Drawing isopleths of E_0^* in an E^*-$1/H^*$ map, enhances the visualization since the points on the same isopleth line should have been subjected to an equal energy efficient treatments [2].

$$E_0^* = P^*/S^*d^*H^* = [AP/(2VdH)][1/\rho C_p(T_m - T_0)] \quad (1.4)$$

1.8 Study objectives

One of the drawbacks in L-PBF is its rather low production rate. The production speed of L-PBF can be enhanced by increasing the values of laser scan speed, hatch distance and layer thickness. Among the three parameters, the effect of increasing layer thickness has the most significant improvement on production speed since it reduces the number of the layers need to be exposed by the laser and the exposure of layers constitute the largest proportion of the production time. The state of the art powder layer thickness used in L-PBF process is in the range of 20-40 μm [11]. For this thesis, the powder layer thickness is increased to 80 μm to increase the productivity and the research hypothesis are formulated as follows:

- The quality of the L-PBF IN718 products such as relative density and surface finish would be compromised due to the high layer thickness used that is more than double of the state of art value.
- Through the optimization of key processing parameters, namely the laser power, scanning speed and hatch distance, one can achieve reasonably good relative density and surface quality despite the significant increase in layer thickness.
- The quality of L-PBF parts depends on the geometrical design as well, which should be accounted for during the experimental optimization process.
- A statistical Design of Experiment (DoE) and regression analysis approach, that are widely applied in many engineering problems, can also be applied to the optimization of processing parameters in L-PBF process.

2

Experimental methods

2.1 Material and L-PBF machine

Gas-atomised IN718 powder supplied by Höganäs was used as the feedstock powder. The commercial name of the product is AMPERPRINT Ni-SA 718 and based on the data sheet provided by the company, the powder is expected to have the chemical composition as shown in table 2.1. The size distribution of the powder particles is expected to be in the range of 15-45 μm.

Table 2.1: Chemical composition of the IN718 powder

	Ni	Cr	Nb	Mo	Ti	Al	C	B	Co	Cu	Mn	N	O	P	S	Si
%	53.8	19.0	5.43	3.0	1.0	0.5	0.04	<0.002	0.0	<0.01	<0.01	0.008	0.018	<0.005	0.002	<0.10

The machine used for the printing is EOS M290, which uses a continuous wave fiber laser with 100 µm laser spot diameter and a Gaussian laser power distribution. The machine has a maximum laser power of 400 Watt [29].

2.2 Design of Experiment

For efficient collection of experimental data, a statistical Design of Experiment (DoE) approach was adopted. An efficient DoE enables the correlation between the response/outcome and the input variables/independent factors based on the results with minimum number of experiments required. In this study, the input variables are selected as laser power, scanning speed and hatch distance. The relative density of L-PBF processed IN718 sample is measured as the outcome. The objective of the investigation is to identify the optimum combination of the input variables that maximizes the relative density of the product. The full factorial design is the most commonly used DoE methods despite the fact that more efficient DoE methods are available. The full factorial design is also called one-factor-at-a-time design, where the value of one factor is varied while other factors are fixed. In the case of a full factorial design, the number of experiment runs needed is according to equation 2.1. For instance, a three-level full factorial DoE for three factors requires a total number of 27 (3^3)runs.

$$Runs = l^k \tag{2.1}$$

where l denotes the number of levels required for each factor, k denotes the number of independent factors for the problem under investigation.

Instead of using a full factorial design, a central composite design (CCD) is employed to reduce the number of required experiments. The number of experimental runs required for a CCD design is according to equation 2.2.

$$Runs = 2^k + 2k + n \tag{2.2}$$

where n denotes the number of replicate points at the centre of the design space. The replicate points are included for the estimation of experimental uncertainties. For each factor, a range of high and low values shall be defined. The CCD design selects experimental conditions in each factor within the defined range. For a given CCD design, a matrix of coded values specifies the layout of the experimental levels. The real-world experimental values for each factor can then be obtained through the conversion as defined in 2.3. In equation 2.3, mean and range are calculated based on the high and low values defined for each parameter. The central point can be defined as the point which shows the coded value of zero for all of the involved factors.

$$Coded\ value = \frac{Real\ value\ -\ Mean}{Range/2} \tag{2.3}$$

The high and low levels used for this design are shown in table 2.2.

Table 2.2: High and low levels of process parameters

Parameter	Laser Power (P) [W]	Scanning speed (S) [mm/s]	Hatch Distance (H) [mm]
Low level	270	800	0.09
High level	330	1200	0.13

2.2.1 Central Composite Design

Central Composite Design (CCD) is one of the most popular second-order DoE, it assists to build a regression model for finding the optimum point in a process through regression analysis. The main difference between CCD and full factorial methods is that the CCD model is capable of estimating second-order effects and interaction between factors with less required experimental runs. A CCD design includes the central point, axial points and star points. The axial points can be defined as points with the distance of α with the central point. In addition, six replicated runs on the central point (highlighted rows of tables 2.3 and 2.4), have been added to evaluate the deviation of the measurement. Substituting k with 3 (number of factors in the current thesis) and n with 6 (number of central replicates for estimation of internal variance) in 2.2, the calculation returns 14 unique combinations of the three factors and 6 central replicates, which amounts to a total number 20 experimental runs.

Using the CCD feature of JMP Pro 14 software and setting the value of α as 1.63 (meaning the axial points are 1.63 away from the central point in coded value), experimental runs of the first batch of samples (C-series) are defined as described in table 2.3.

Table 2.3: Parameters variation among C-series samples

Sample	Power (P) [W]	Scanning speed (S) [mm/s]	Hatch distance (H) [mm]
C-1	270	800	0.09
C-2	270	1200	0.13
C-3	300	1000	0.11
C-4	330	1200	0.09
C-5	300	1000	0.11
C-6	330	800	0.13
C-7	270	1200	0.09
C-8	330	1200	0.13
C-9	300	1000	0.11
C-10	270	800	0.13
C-11	330	800	0.09
C-12	300	1000	0.11
C-13	300	1000	0.11
C-14	300	1000	0.14
C-15	300	673	0.11
C-16	300	1327	0.11
C-17	349	1000	0.11
C-18	300	1000	0.11
C-19	251	1000	0.11
C-20	300	1000	0.08

In the second experimental campaign (T-series), a slightly enlarged range of the parameters were applied by selecting an α value of 1.68. In addition, eight extra points were added to the experimental matrix for observation of the extreme conditions. The experimental runs of T-series, are shown in table 2.4.

Table 2.4: Experimental runs, T-series

Sample	Power (P) [W]	Scanning speed (S) [mm/s]	Hatch distance (H) [mm]
T-1	270	800	0.09
T-2	270	1200	0.13
T-3	300	1000	0.11
T-4	330	1200	0.09
T-5	300	1000	0.11
T-6	330	800	0.13
T-7	270	1200	0.09
T-8	330	1200	0.13
T-9	300	1000	0.11
T-10	270	800	0.13
T-11	330	800	0.09
T-12	300	1000	0.11
T-13	300	1000	0.11
T-14	300	1000	0.14
T-15	300	673	0.11
T-16	300	1327	0.11
T-17	349	1000	0.11
T-18	300	1000	0.11
T-19	251	1000	0.11
T-20	300	1000	0.08
T-21	250	664	0.08
T-22	250	1336	0.14
T-23	250	664	0.14
T-24	250	1336	0.08
T-25	350	1336	0.14
T-26	350	664	0.14
T-27	350	1336	0.08
T-28	350	664	0.08

2.2.2 Sample geometry

The first twenty samples (C-series) were printed in a conventional cubic shape with the dimension of $10 \times 10 \times 10$ $[mm^3]$. As shown in figure 2.1, each sample was cut twice, providing both vertical and horizontal cross-sections for the porosity assessment. The vertical and horizontal cuts were performed at 2 and 2.5 mm distances from the side surface and the top surface, respectively.

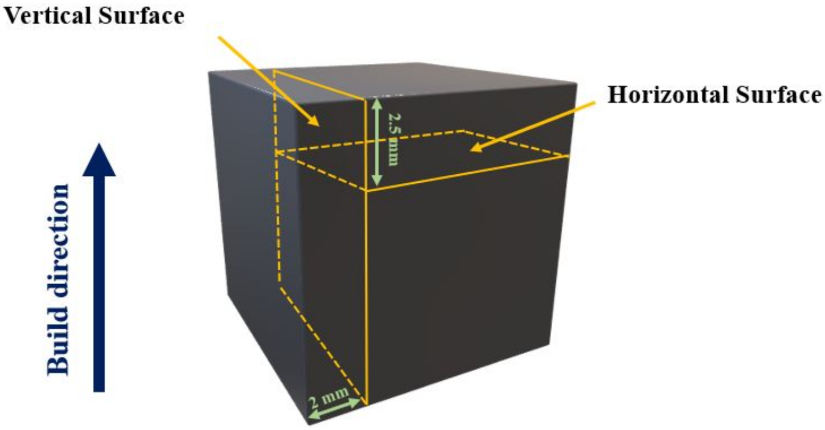

Figure 2.1: Schematic drawing of the performed cuts on C-series

In the second experimental campaign (T-series), more complex designs (staircase geometry as show in figure 2.2) were used to characterize the influence of geometry on the part quality (relative density and surface roughness). As shown in the figure 2.2, for observation of horizontal and vertical surfaces two different samples for each set of parameters were produced. Cut performed on each specimen for sample preparation are illustrated in figure 2.2. The cut was made in the middle of the specimens with ca. 7.5 and 6 mm distance from edges in horizontal and vertical samples, respectively.

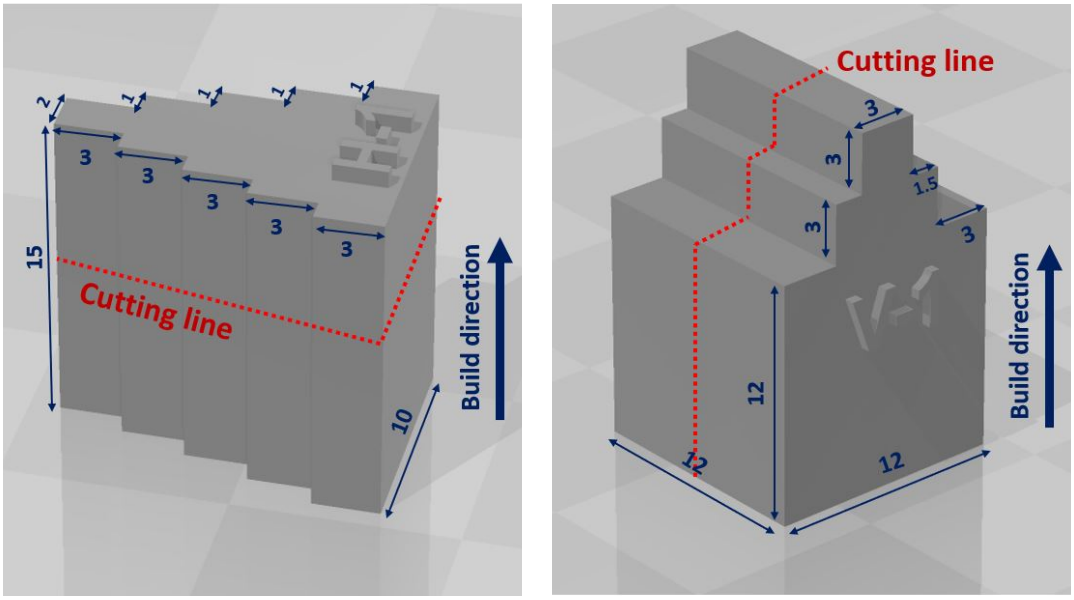

(a) Horizontal sample

(b) Vertical sample

Figure 2.2: T-series samples' geometry - dimensions are in millimeter

2.3 Analysis

For the porosity measurement through image analysis, all of the 48 samples described in sections 2.2.1 - 2.2.2 were subjected to the sample preparation steps as follows. The machine and cutting wheel used for the cutting were BUEHLER ISOMET2000 and an aluminum oxide cut-off wheel 50A13. The mounting was performed using a Struers (CitoPress-20) machine, while applying DuroFast resin for optical microscopy samples and PolyFast for SEM samples. Grinding and polishing were applied using a Struers (TegraPol-31) machine. The steps applied can be found in table 2.5.

Table 2.5: Grinding and polishing steps applied on the samples

	Surface	Time [minutes]	Force [N]	rpm	Suspension/Lubricant
PG	SiC foil 220	5	15	300	Water
FG	MD-Largo	5	15	150	DiaPro Allegro/Largo [9μm]
DP1	MD-Dac	5	15	150	DiaPro Dac [3μm]
DP2	MD-Nap	1	15	150	DiaPro Nap [1μm]

To reveal the microstructure and melt pools, an electrochemical etching was performed on selected samples using a solution of 10g/100ml of oxalic acid.

2.3.1 Image Analysis

Prepared samples contained both vertical and horizontal cross-sections. Images were taken from both cross-sections using a ZEISS-Axio-Imager.M2m optical microscope. The images from both vertical and horizontal surfaces were analyzed by ImageJ software. The ImageJ software evaluates the areal fraction of pores in each image, from which the area fraction of solidified material is obtained as a 2D equivalent of relative density. The relative density was calculated according to the densities measured from both horizontal and vertical cross-sections as shown in equation 2.4. In equation 2.4, D_r, D_H, and D_V are relative density, the density of the horizontal cross-section and density of the vertical cross-section, respectively. In order to observe the shape of the pores and their correlation with melt pools, optical image of etched samples was used.

$$D_r = \sqrt{D_H^2 + D_V^2} \tag{2.4}$$

For T- series and in order to see the geometrical effect on the final density of the part, the image analysis was conducted separately on each section of vertical and horizontal cross-sections. In other words, based on the thickness and as illustrated in figure 2.3, horizontal and vertical surfaces were divided into 5 and 3 sections, respectively. For T-series and calculation of relative density explained in equation 2.4, D_H and D_V, are the average of densities calculated for each section.

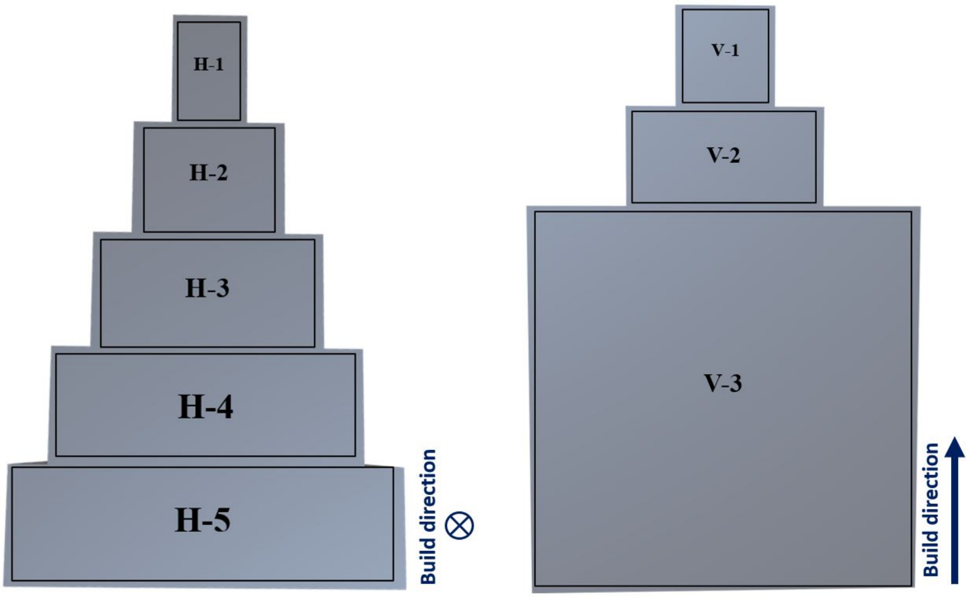

(a) Horizontal plane - 5 sections **(b)** Vertical plane - 3 sections

Figure 2.3: Section designation of T-series based on the printed thickness

The optical images of the T-series samples were also used for roughness measurement by applying an interfacial roughness profile graph in ImageJ software. A similar procedure has been used by authors of [30]. As the first step, the global scale was set and applied to all the images of the same format. Secondly, a fixed Region Of Interest (ROI) was defined to contain the right edge of section 1 (named as H-1 and V-1 in figure 2.3). The dimensions of the applied ROI is 0.7 × 2.5 mm. Finally, *Analyze stripes V2.6* plugin was performed on this ROI for each picture, the edge profile of the cross-sections were extracted and analyzed, resulting in the measurements of Root Mean Squared (RMS) edge roughness (Rq) and peak-to-peak edge roughness (Rt) in μm. Rq is equal to root mean squared of the distance between each peak and valley from the mean line divided by the length of the area. Rt refers to the highest distance between a peak and a valley. Rq and Rt measurements are shown schematically in figure 2.4. In this roughness measurement, further to the indication of ROI, the plugin makes it possible to adjust the threshold manually to define the edge of the sample more accurately. Depending on the magnification used and the threshold adjustment, the results may show a lack of reliability.

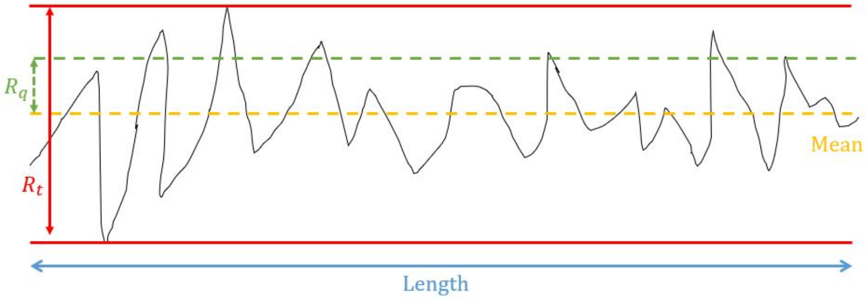

Figure 2.4: Schematic explanation of Rq and Rt

2.3.2 Regression Analysis

The obtained relative densities have been subjected to a regression analysis using both R-studio and JMP software. The aim of the regression analysis is to achieve the model for prediction of the final density based on process parameters and indication of the significant variables. In addition, the goodness-of-fit and significance of the obtained model were examined by R-squared and P-value, respectively.

The observed relative density of eight points limited to high and low levels of parameters, lead in solving the below matrix and can be presented in a simple linear model as shown in equation 2.5. In this equation, b_0 represents the intercept or baseline for the linear model. b_P, b_S and b_H represent the effect of laser power, scanning speed, and hatch distance, respectively. In addition, the interaction effect between parameters has been taking into account represented by $b_{P,S}$, $b_{S,H}$, $b_{P,H}$ and $b_{P,H,S}$.

The resulting model from CCD design shall provide the coefficients of equation 2.6 which includes the quadratic additionally. In equation 2.6, $b_{P,P}$, $b_{S,S}$ and $b_{H,H}$ represent the effect of quadratic terms.

$$\begin{pmatrix} D_1 \\ D_2 \\ D_3 \\ D_4 \\ D_5 \\ D_6 \\ D_7 \\ D_8 \end{pmatrix} = \begin{pmatrix} -1 & -1 & -1 \\ +1 & -1 & -1 \\ -1 & +1 & -1 \\ +1 & +1 & -1 \\ -1 & -1 & +1 \\ +1 & -1 & +1 \\ -1 & +1 & +1 \\ +1 & +1 & +1 \end{pmatrix} \times \begin{pmatrix} b_0 \\ b_P \\ b_S \\ b_H \\ b_{P,S} \\ b_{S,H} \\ b_{P,H} \\ b_{P,H,S} \end{pmatrix}$$

$$D = b_0 + b_P P + b_S S + b_H H + b_{P,S} P.S + b_{S,H} S.H + b_{P,H} P.H + b_{P,H,S} P.H.S \tag{2.5}$$

$$\begin{split} D = b_0 + b_P P + b_S S + b_H H + b_{P,S} P.S + b_{S,H} S.H + b_{P,H} P.H + b_{P,P} P^2 + b_{S,S} S^2 \\ + b_{H,H} H^2 \end{split} \tag{2.6}$$

3

Results and discussion

3.1 Porosity measurement

3.1.1 C-series

Using the interactive tile tool of the optical microscope and as described in section 2.3, a full image of both vertical and horizontal surfaces of each sample was obtained. The results achieved from using ImageJ software on these images, have been illustrated in table 3.1. It can be seen that almost the same results have been achieved for the replicated experimental highlighted in table 3.1, indicating a good repeatability of the experiments. In addition, some of the pictures taken for this analysis are shown in figure 3.1. The standard deviation calculated for the replicated samples equals to 0.0033 %.

Table 3.1: Porosity results of C-series

Sample	P [W]	S [mm/s]	H [mm]	Porosity [%]		Relative density [%]
				Vertical plane	Horizontal plane	
C-1	270	800	0.09	0.047	0.084	99.96
C-2	270	1200	0.13	4.954	2.734	95.38
C-3	300	1000	0.11	0.044	0.041	99.94
C-4	330	1200	0.09	0.027	0.037	99.95
C-5	300	1000	0.11	0.073	0.151	99.95
C-6	330	800	0.13	0.032	0.043	99.94
C-7	270	1200	0.09	0.142	0.016	99.96
C-8	330	1200	0.13	1.201	2.563	96.90
C-9	300	1000	0.11	0.128	0.031	99.94
C-10	270	800	0.13	0.079	0.040	99.93
C-11	330	800	0.09	0.029	0.036	99.95
C-12	300	1000	0.11	0.099	0.076	99.94
C-13	300	1000	0.11	0.077	0.026	99.95
C-14	300	1000	0.14	0.601	0.495	99.18
C-15	300	673	0.11	0.041	0.063	99.93
C-16	300	1327	0.11	0.375	0.289	99.48
C-17	349	1000	0.11	0.012	0.020	99.98
C-18	300	1000	0.11	0.048	0.051	99.95
C-19	251	1000	0.11	0.142	0.052	99.85
C-20	300	1000	0.08	0.340	0.030	99.96

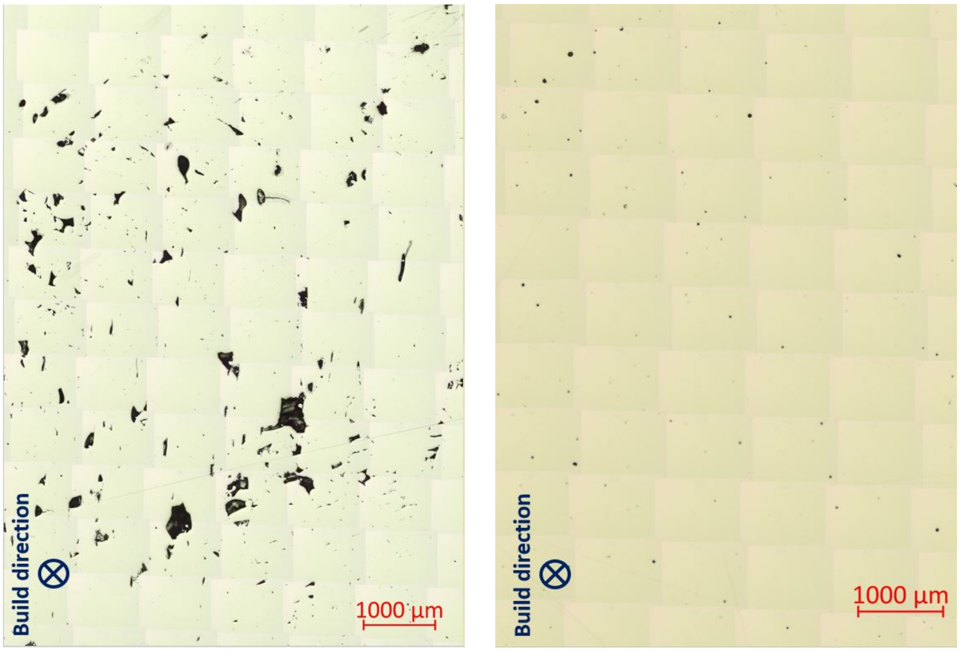

(a) Sample C-8, Horizontal plane **(b)** Sample C-15, Horizontal plane

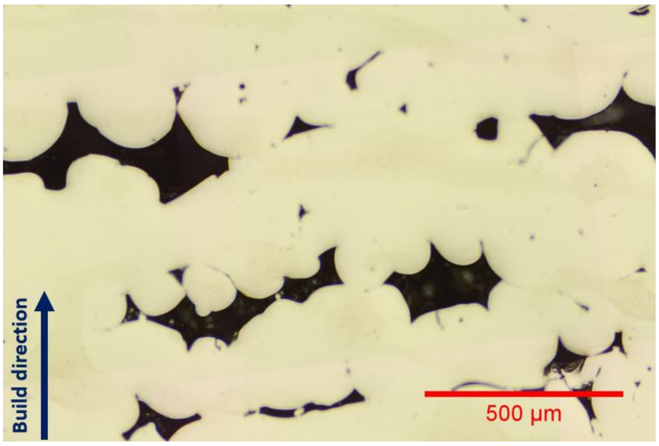

(c) Sample C-2, Vertical plane

Figure 3.1: Optical images taken from C-series

As described in the Table 3.1, almost all of the samples show a rather high relative density of over 99.9%. Samples number C-2 and C-8 show the highest amount of pores. In those two cases, the high scanning speed is combined with large hatch distance, resulting in significant lack of fusion between hatches and layers and accordingly higher porosity level. It is interesting that although the power changes from its lowest value in sample C-2 to its highest value in sample C-8, it is not effective enough to compensate for lack of fusion induced by fast scanning speed and large hatch distance.

In order to reveal the shape of the melt pool and where the pores are located relative to the melt pools, optical images of samples number C-2, C-8, C-11, C-13, C-17, and C-20 were taken after etching, as shown in the figure 3.2. It can be seen that as the higher energy input (higher power/lower scanning speed/ lower hatch distance) is applied, the pore' type changes from irregular shaped lack of fusion located (e.g C-2) at the melt pool boundaries into widely distributed and rather small spherical pores (e.g C-17). On the other hand, the number small spherical pores formation can be assumed to be increased when too high energy input is applied which can be correlated with the higher possibility of disturbance of the melt pool and gas pores getting trapped inside the melt pools.

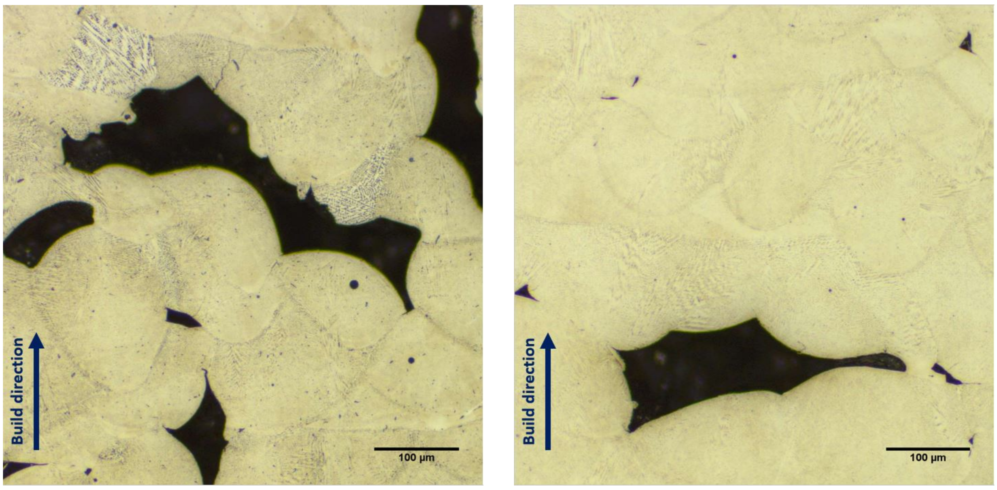

(a) Sample C-2, Vertical plane **(b)** Sample C-8, Vertical plane

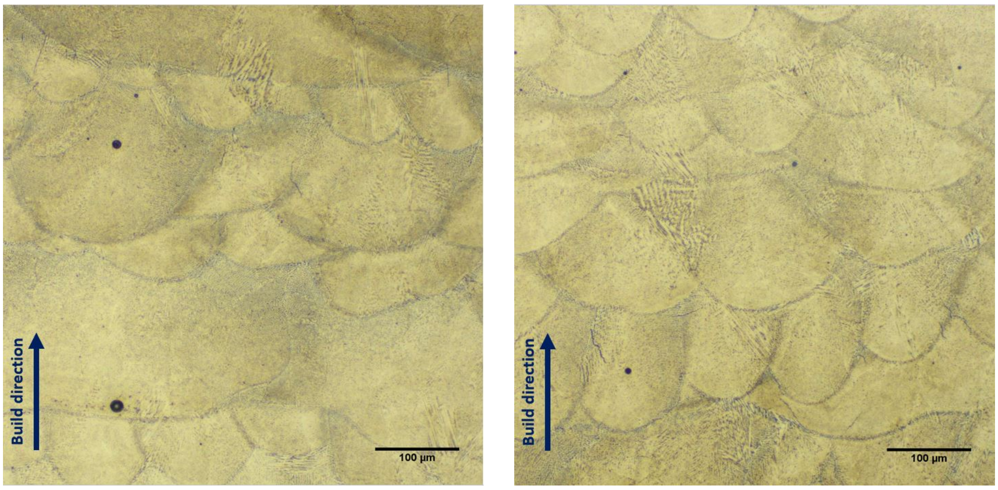

(c) Sample C-11, Vertical plane **(d)** Sample C-13, Vertical plane

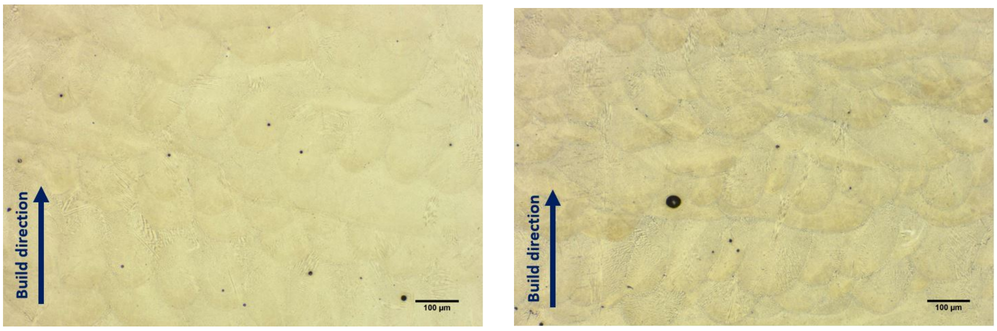

(e) Sample C-17, Vertical plane **(f)** Sample C-20, Vertical plane

Figure 3.2: Optical images from etched C-series samples

3.1.2 T-series

The image analysis of T-series, as described in section 2.3, was performed on each section of the horizontal and vertical cross-sections. The summarized results for T-series can be found in table 3.2. In table 3.2, average porosity is the average of porosity in five sections of the horizontal plane and three sections of the vertical plane. In addition, the replicated samples are highlighted and the results of them show a 0.0472 % standard deviation. The detailed results including the porosity result of each geometrical section are illustrated in tables A.1 to A.6 of appendix 1.

Overall, it appears that the central point of the DoE hit close to the optimum processing window since the central replicates consistently show sound relative densities.

Table 3.2: Porosity results of T-series

Sample	P [W]	S [mm/s]	H [mm]	Average porosity [%]		Relative density [%]
				Horizontal	Vertical	
T-1	270	800	0.09	0.037	0.026	99.95
T-2	270	1200	0.13	4.847	5.310	92.81
T-3	300	1000	0.11	0.071	0.059	99.91
T-4	330	1200	0.09	0.046	0.026	99.95
T-5	300	1000	0.11	0.092	0.068	99.89
T-6	330	800	0.13	0.049	0.033	99.94
T-7	270	1200	0.09	0.051	0.089	99.90
T-8	330	1200	0.13	1.002	1.301	98.36
T-9	300	1000	0.11	0.067	0.026	99.93
T-10	270	800	0.13	0.071	0.103	99.87
T-11	330	800	0.09	0.044	0.025	99.95
T-12	300	1000	0.11	0.105	0.134	99.83
T-13	300	1000	0.11	0.033	0.026	99.96
T-14	300	1000	0.14	0.641	1.192	98.65
T-15	300	673	0.11	0.100	0.083	99.87
T-16	300	1327	0.11	0.844	1.013	98.68
T-17	349	1000	0.11	0.045	0.034	99.94
T-18	300	1000	0.11	0.024	0.044	99.95
T-19	251	1000	0.11	0.286	0.321	99.57
T-20	300	1000	0.08	0.055	0.035	99.93
T-21	250	664	0.08	0.273	0.238	99.64
T-22	250	1336	0.14	19.137	18.429	73.43
T-23	250	664	0.14	0.088	0.131	99.84
T-24	250	1336	0.08	0.085	0.047	99.90
T-25	350	1336	0.14	2.480	2.633	96.38
T-26	350	664	0.14	0.046	0.045	99.94
T-27	350	1336	0.08	0.036	0.029	99.95
T-28	350	664	0.08	0.456	0.483	99.33

Examples of the images used for porosity measurement are shown in figure 3.3. Similar to the C-series, the lower energy input (e.g T-2, T-8, T-22 and T-25) results in irregularly shaped lack of fusion pores, while too high energy input (e.g T-28) leads to widely distributed and rather small spherical pores. It is worthy to mention that the varied sample thickness in T-series has additional implications for the process parameters investigated. It is evident that the thinner sections are more sensitive to high energy input since the number of pores increase from section 3 to 1 in vertical cross-section and from 5 to 1 in horizontal cross section of sample T-28.

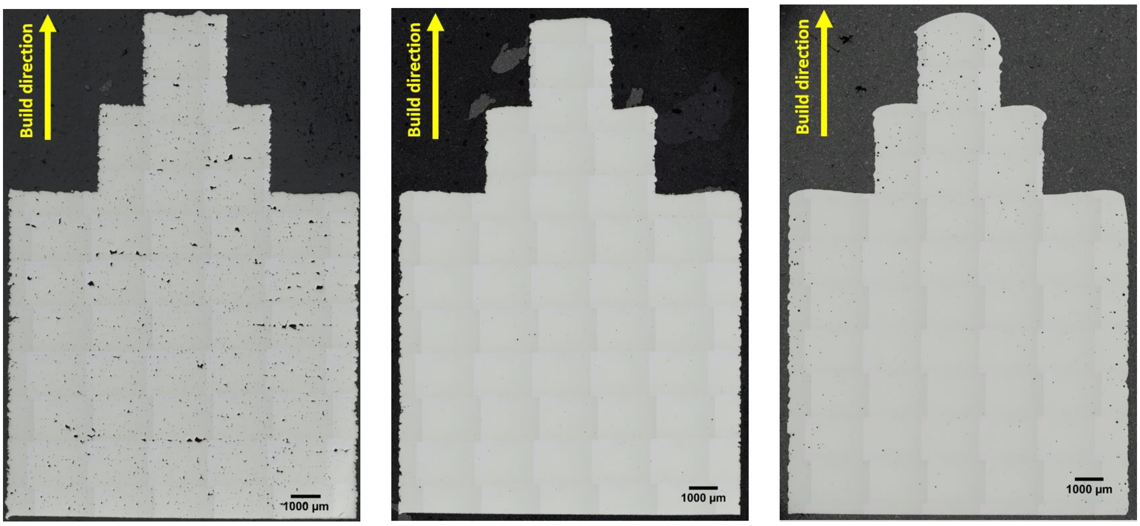

(a) Sample T-8 Vertical plane **(b)** Sample T-17 Vertical plane **(c)** Sample T-28 Vertical plane

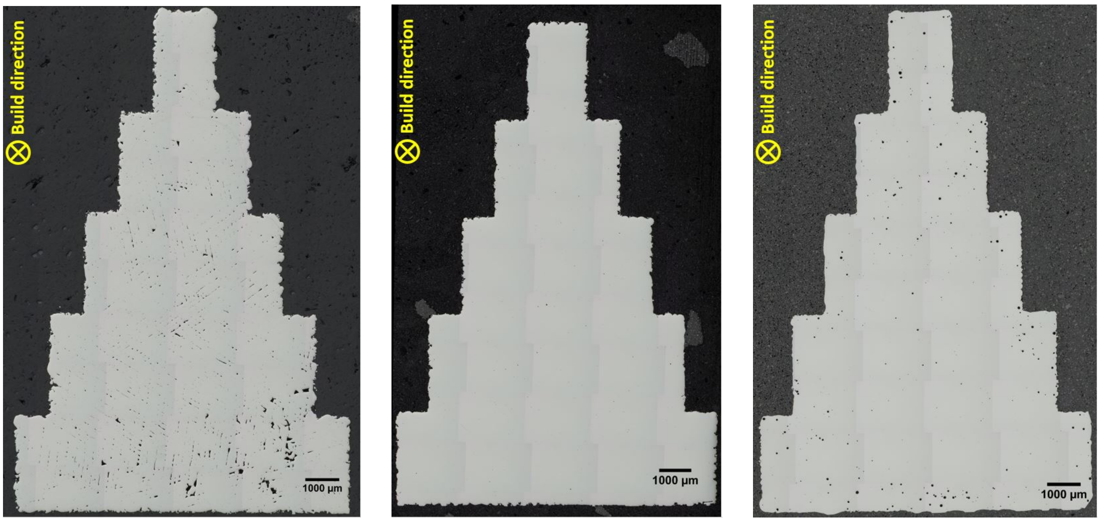

(d) Sample T-8 Horizontal plane **(e)** Sample T-17 Horizontal plane **(f)** Sample T-28 Horizontal plane

Figure 3.3: Optical images from T-series samples

Some of the etched samples for the melt pool and microstructure observations are shown in figure 3.4. As shown in figure 3.4, too high energy input (e.g sample T-28) leads to an over-melted microstructure with deep melt pools stretched along the build direction, while in the central replicate samples (e.g sample T-5 of figure 3.4) where the processing parameters are considered to yield optimum energy input, the melt pools are of similar depths and widths and only small amount of pores are found. Moreover, the high energy input applied in sample T-28 as shown in 3.4 (a) has a curved edge profile, indicating a worse geometrical compliance.

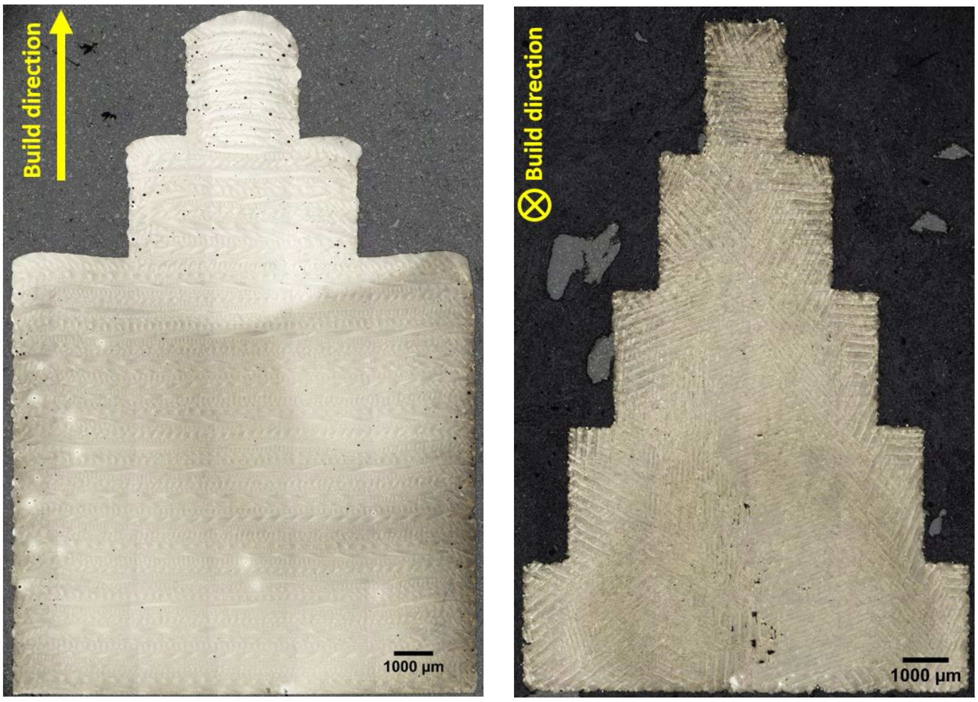

(a) Sample T-28 Vertical plane **(b)** Sample T-19 Horizontal plane

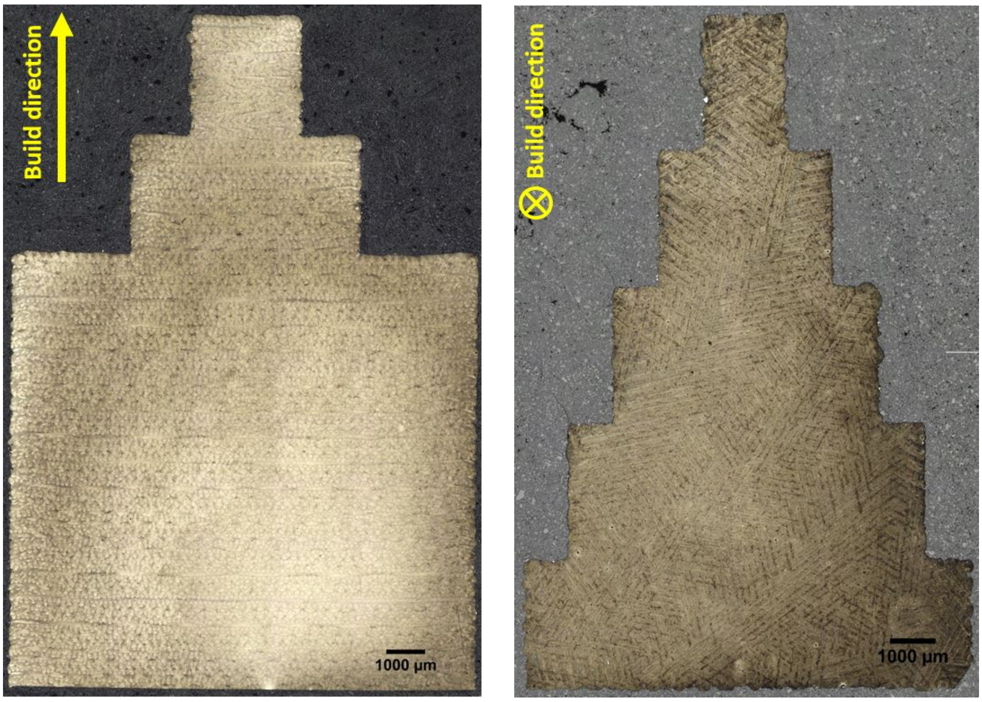

(c) Sample T-5 Vertical plane **(d)** Sample T-23 Horizontal plane

Figure 3.4: Optical images from etched T-series samples

In order to evaluate the geometrical effect on the porosity of the final product, average porosity in each section was calculated and summarized in figure 3.5. As shown in the graphs in figure 3.5, the average calculated porosity is higher in section 2 of both vertical and horizontal planes. The observed higher average relative porosity in section 2, can be the result of a deviation in the measurements or the fact that thinner area might be more prone to melt pool disturbance.

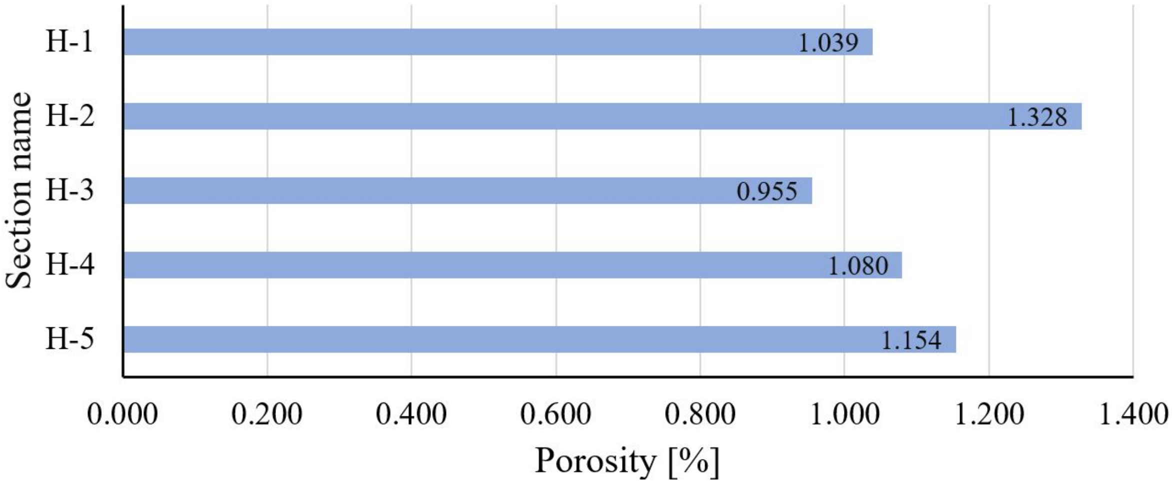

(a) Vertical planes

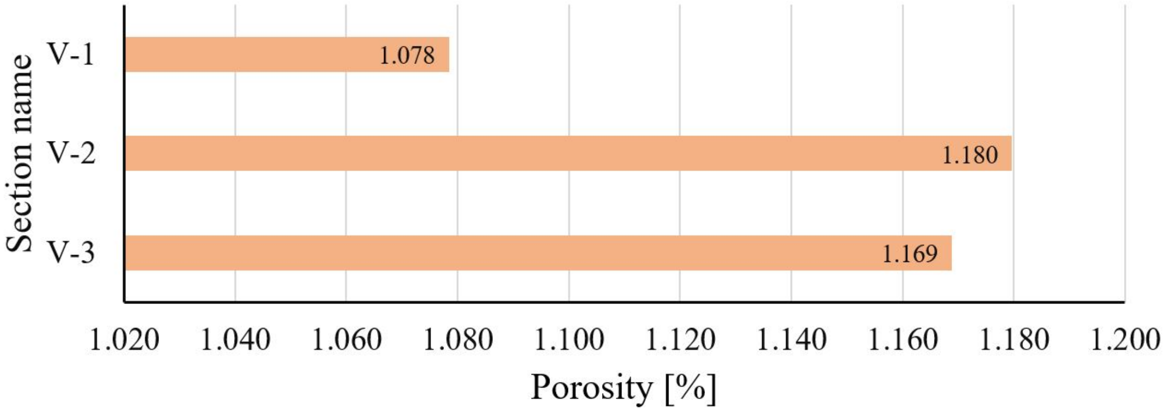

(b) Horizontal planes

Figure 3.5: Geometrical effect on the porosity in T-series

3.2 Surface roughness

As described in section 2.3, the R_q and R_t were measured for T-series. The result for section 1 of each horizontal and vertical plane (as shown in figure 2.3), are illustrated in table 3.3. The replicated samples are highlighted in table 3.3. The detailed results of surface roughness observed in each geometrical section are shown in tables A.1 to A.6 of appendix 1. In addition, an average surface roughness of different sections was calculated for each horizontal and vertical plane. The obtained average surface roughness for each horizontal and vertical plane was used to study the correlation of the surface roughness with the applied VED. Similar to the trend in relative density in response to VED increase, there seems to be an optimum window of VED where the surface roughness reaches its minimum. As shown in figure 3.6, in the low VED regime, the roughness is high and then decreases with increasing VED whereas the roughness increases slightly in the high VED regime with a different appearance on the edge profile. It can be concluded that both the porosity formation and the surface roughness follow a similar behaviour with variation of VED: (1) at low VED (less than 34 [J/mm^3]), lack of fusion leads to high amount of porosity and rough surfaces. (2) The fluid flow within the melt pool stabilizes at medium VED regime (34-50 [J/mm^3]) leading to achieve full densification and less surface roughness. (3) In the too high VED regime (above 50 [J/mm^3]), the excessive energy input imposed by the laser, promotes evaporation and volatile gas flow thus introducing gas pores into the bulk of the sample.

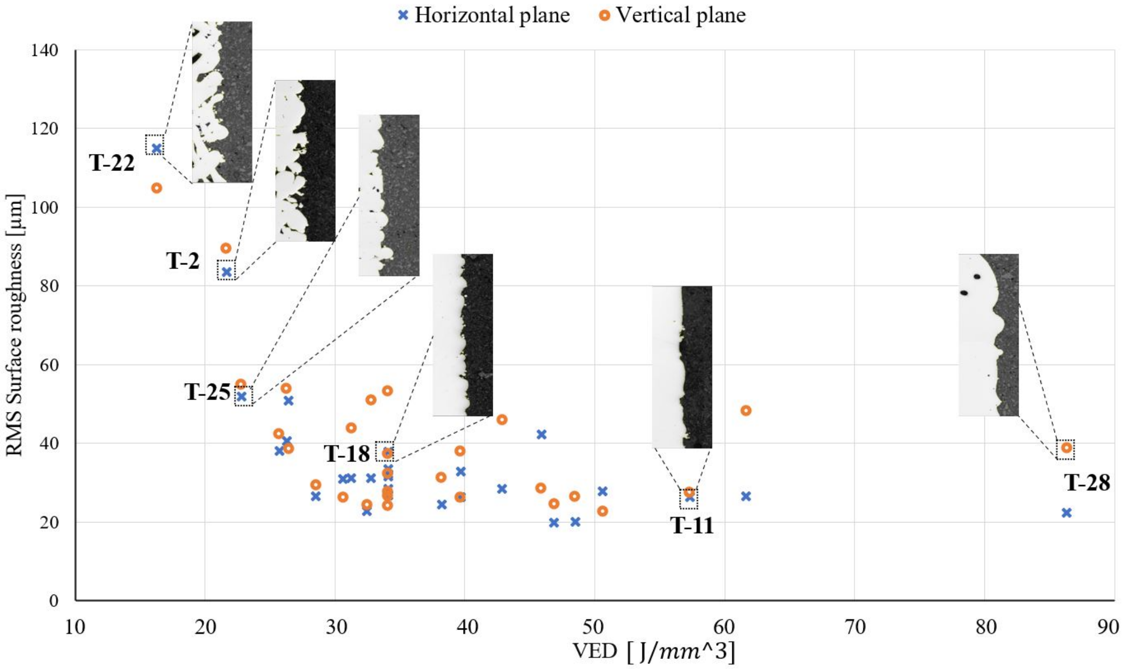

Figure 3.6: Correlation between surface roughness and the applied VED in T-series

Table 3.3: Surface roughness results of T-series in section 1 of each horizontal and vertical plane

Sample name	**RMS edge roughness (R_q) [µm]**		**peak-to-peak edge roughness (R_t) [µm]**	
	Horizontal Plane	**Vertical plane**	**Horizontal Plane**	**Vertical plane**
T-1	30.5	41.5	146.1	215.9
T-2	97.0	54.4	402.3	359.2
T-3	53.0	16.2	210.3	147.3
T-4	20.5	47.0	141.9	223.2
T-5	39.2	24.0	177.4	129.1
T-6	29.5	34.6	158.8	178.1
T-7	47.7	54.3	229.5	274.6
T-8	38.1	28.5	196.7	229.2
T-9	19.9	19.5	150.7	146.0
T-10	37.3	35.3	174.5	170.8
T-11	30.7	31.2	157.5	192.6
T-12	24.1	41.3	130.1	218.1
T-13	57.8	69.6	244.9	308.8
T-14	21.4	25.3	112.6	135.9
T-15	52.2	37.4	250.0	167.5
T-16	50.4	37.9	292.9	187.0
T-17	35.9	36.9	195.3	192.9
T-18	34.7	43.8	186.8	201.8
T-19	26.4	20.0	143.0	157.5
T-20	15.3	23.9	123.6	140.4
T-21	28.2	39.4	209.1	212.4
T-22	106.5	77.2	496.3	406.9
T-23	82.2	58.7	457.4	376.9
T-24	6.6	28.5	30.4	142.9
T-25	58.7	38.5	284.9	276.2
T-26	32.3	33.5	153.2	216.2
T-27	28.3	71.4	267.9	353.9
T-28	18.0	33.9	137.6	236.6

3.3 Regression analysis of the results

In order to obtain a model to predict optimum conditions resulting in the highest densities, a regression analysis was performed. In addition, based on the number of experimental runs and the range of the variables used, the most significant terms affecting the outcome (density) can be determined. As described in chapter 2, the accuracy and statistical significance of the regression model are verified based on the R-squared value and the P-value. Models were built using both R-studio and JMP software to cross-check the outcomes.

3.3.1 R-Studio Model

Using R-studio for analysing the results in table 3.1 and 3.2, regression models are obtained for C-series and T-series as shown in equations 3.1 and 3.2, respectively. In equations 3.1 and 3.2, the P, S and H values shall be used in coded values explained equation 2.3 of section 2.2. The R-squared values for the C-series and T-series were as high as 0.79 and 0.83, meaning 79 percents and 83 percents of the variance observed in experiments can be accounted for by the regression models for C-series and T-series respectively. In addition, the P-values obtained are 0.0165 for C-series and 2.601×10^{-5} for T-series, indicating that the statistical significance of the model is improved from C-series to T-series due to the slight change in DoE matrix and the addition of eight extra samples. The detailed result of R-Studio is available in the appendix section A.2.

$$\begin{split} D = 99.9894 + 0.1292P - 0.6256S - 0.6719H + 0.1906P.S - 0.9496S.H + 0.1916P.H \\ -0.1761P^2 - 0.2540S^2 - 0.3042H^2 \end{split} \tag{3.1}$$

$$\begin{split} D = 100.2589 + 1.2444P - 1.6577S - 1.6712H + 0.9955P.S - 1.3335S.H + 0.9993P.H \\ -0.3634P^2 - 0.5468S^2 - 0.5410H^2 \end{split} \tag{3.2}$$

The Pareto plots of models are shown in figures 3.7 and 3.8. Pareto plot visualizes the relative significance of the variables and the directions (positive or negative) in which the variables affect the outcome (relative density). For the C-series as illustrated in figure 3.7, scanning speed (S) and hatch distance (H) and the interaction of them (S:H) are the most significant variables of the model. This confirms the findings of sections 3.1 in which it was concluded that from sample C-2 to sample C-8, the higher energy input associated with higher applied laser power can not compensate the effect of the more significant terms (scanning speed, hatch distance and their interaction). In other words, the high scanning speed and large hatch distance introduces lack of fusion due to the hydrodynamic instabilities in the melt pool which cannot be eliminated by higher laser power input. Although, in figure 3.8, as the range of power becomes wider in the T-series, the significance of power (P) increases, it still is out ranked by effect of the scanning speed, hatch distance and their interaction.

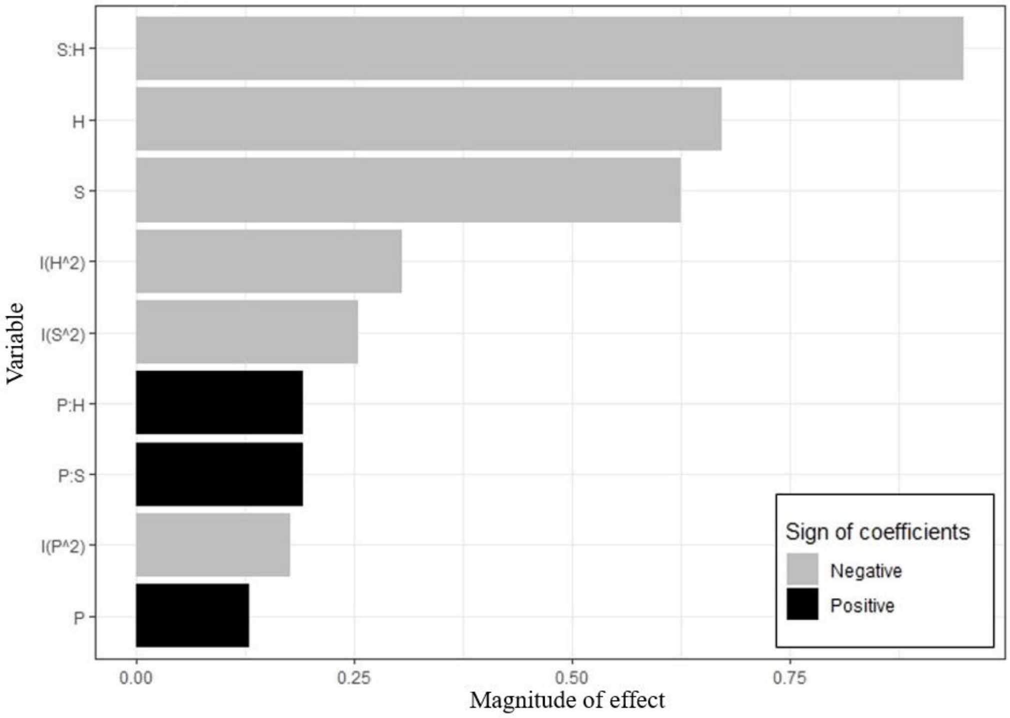

Figure 3.7: Pareto plot for C-series model

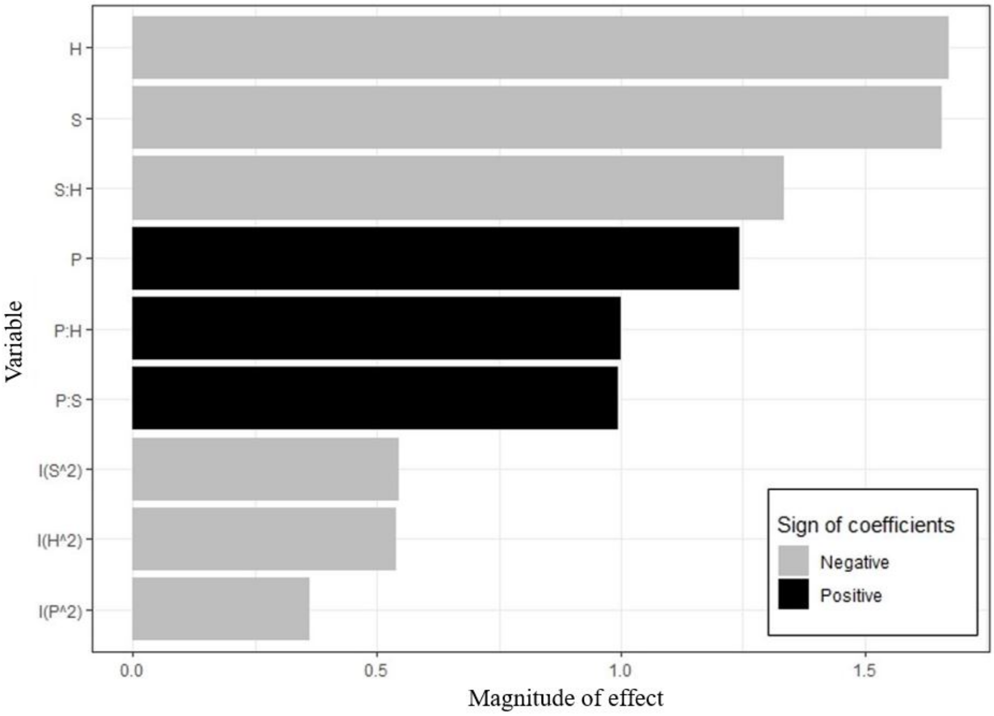

Figure 3.8: Pareto plot for T-series model

3.3.2 JMP Model

Equations 3.3 and 3.4 describe the models built using JMP software with the personality of Standard Least Squares and the same results as described in table 3.1 and 3.2, respectively. The P-value of the models illustrated in 3.3 and 3.4 are 0.49 for C-series and 0.0002 for T-series. R-squared reported for the C-series is 0.53 which increases to 0.78 for the T-series.

$$D = 99.4141 + 0.2768P - 0.3944S - 0.4058H + 0.4897P.S - 0.652S.H + 0.4585P.H + 0.0445P^2 + 0.0421S^2 + 0.0432H^2 \tag{3.3}$$

$$D = 100.2014 + 1.2209P - 1.5875S - 1.6707H + 1.0083P.S - 1.4578S.H + 1.0984P.H - 0.5009P^2 - 0.5299S^2 - 0.4330H^2 \tag{3.4}$$

Proceeding with Stepwise personality of the model instead of Standard Least Squares following by P-value threshold as the stopping rule, results in the indication of significant terms and a new model based on those selected variables. For C-series, the significant terms would be defined as previously shown by R-studio model which are scanning speed, hatch distance and their interaction. By limiting the model terms only to scanning speed, hatch distance, and their interaction the equation 3.3 can be re-written as described in equation 3.5. Applying the Stepwise analysis decreases the R-squared from 0.53 to 0.28 for equation 3.5.

$$D = 99.5005 - 0.3944S - 0.4058H - 0.652S.H \tag{3.5}$$

For T-series, the significant terms indicated by Stepwise analysis are all of the variables except the quadratic term specified to hatch distance. The new Stepwise model built for T-series is expressed in equation 3.6. Applying the Stepwise analysis decreases the R-squared from 0.78 to 0.76 for the equation 3.5. In all of the obtained models, most significant variables are scanning speed and hatch distance.

$$D = 99.7471 + 1.2209P - 1.5875S - 1.6707H + 1.0083P.S - 1.4578S.H + 1.0985P.H - 1.0492S^2 \tag{3.6}$$

3.4 Process development

The obtained result may be used for process development and determination of the proper process parameters for AM of IN718 in an independent format from the machine used. As described in section 1.7, different approaches such as Volumetric Energy Density (VED) and Dimensionless energy per unite volume (E^*), shall be applied to achieve a process map.

3.4.1 Volumetric Energy Density

By plotting the density results for both series vs VED calculated based on equation 1.1, figure 3.9 is obtained. Figure 3.9 is plotted using Fit Y by X feature of JMP software.

Figure 3.9 confirms that keeping VED in the range of 34-50 [J/mm^3] may lead to near to optimum microstructure which contains relatively lower amount of porosity.

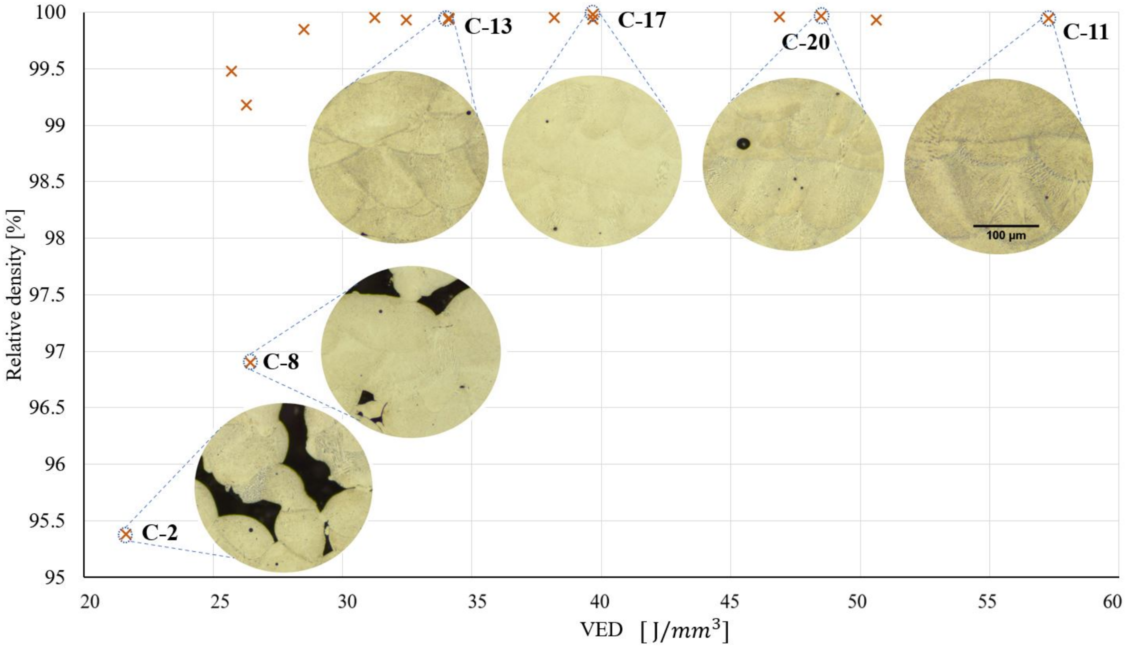

(a) C-series

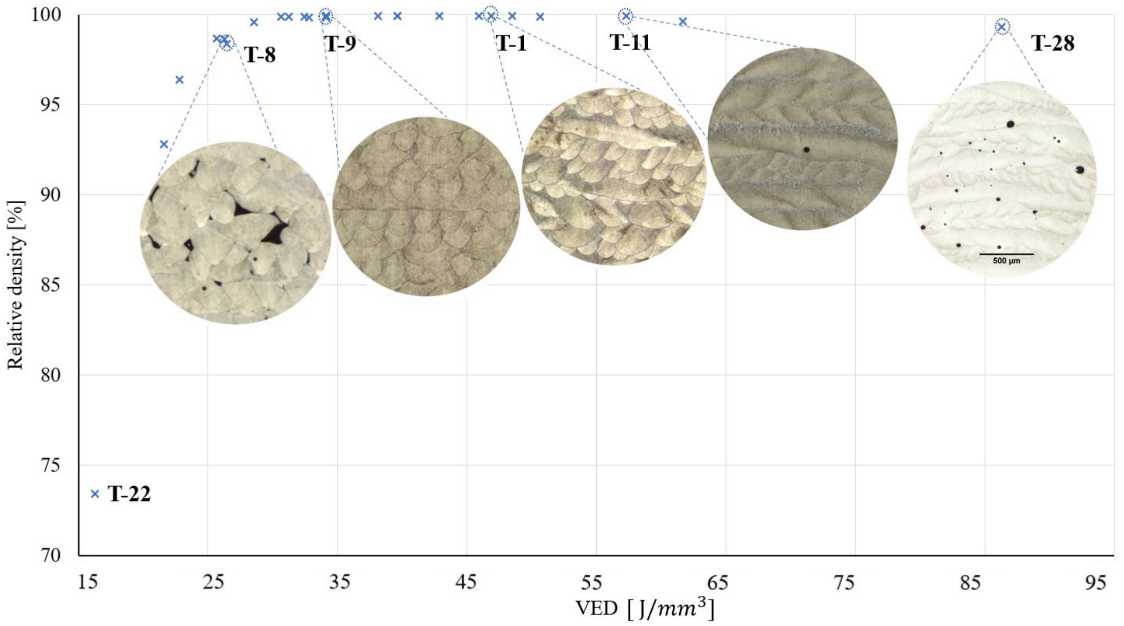

(b) T-series

Figure 3.9: Density vs. VED

3.4.2 Dimensionless energy per unite volume

As described in section 1.7.2, plotting the results based on normalized variables, shall provide a map which can be considered as independent from the AM machine's specifications. The aim of this process mapping is to achieve a 2-D process window to demonstrate the areas associated with normalized process parameters in which rather high densities can be obtained. As the first step for calculation of dimensionless energy per unite volume (E^*), process parameters which are used in equations 1.2-1.4, shall be defined as shown in table 3.4.

Table 3.4: Process parameters used in equations 1.2-1.4

Absorptivity (A)	Density (ρ) $[g/cm^3]$	Specific heat capacity (Cp) $[J.g^{-1}.K^{-1}]$	T$_0$ [°C]	T$_m$ [°C]
≈0.3	8.19	0.435	80	1260

By applying process parameters presented in table 3.4, new sets of data for both C-series and T-series can be defined as illustrated in table A.7 and A.8 of the appendix 1, respectively. Based on the data presented in table A.7 and A.8, contour maps can be plotted as shown in figures 3.10 and 3.11. It can be concluded from the figures 3.10 and 3.11 that densities close to 99.9% can be guaranteed when applying H^* below 2 and E^* above 2.8.

New models can be fitted into this dimensionless set of data which are illustrated in equations 3.7 and 3.8. The resulted P-value for models described in equations 3.7 and 3.8 are 0.0179 and 0.0094, respectively. In addition, obtained R-squared are 0.38 for C-series and 0.31 for T-series.

$$D = 99.593 + 2.594\ \log(E^*) + 3.441\ \log(1/H^*) \tag{3.7}$$

$$D = 96.282 + 8.363\ \log(E^*) + 8.199\ \log(1/H^*) \tag{3.8}$$

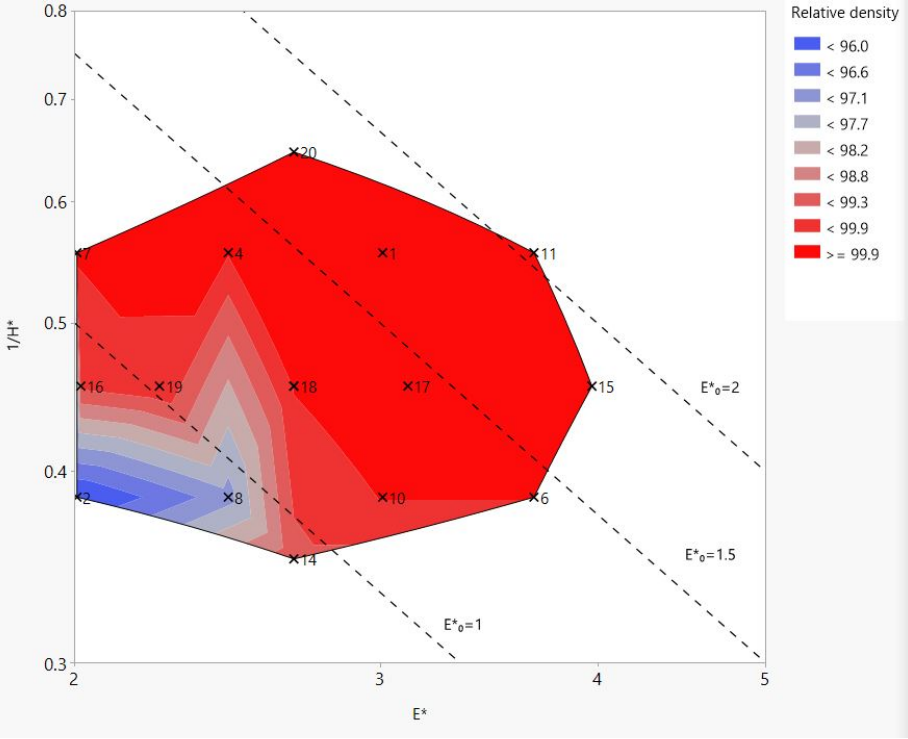

Figure 3.10: Contour plot from JMP software based on dimensionless parameters in C-series

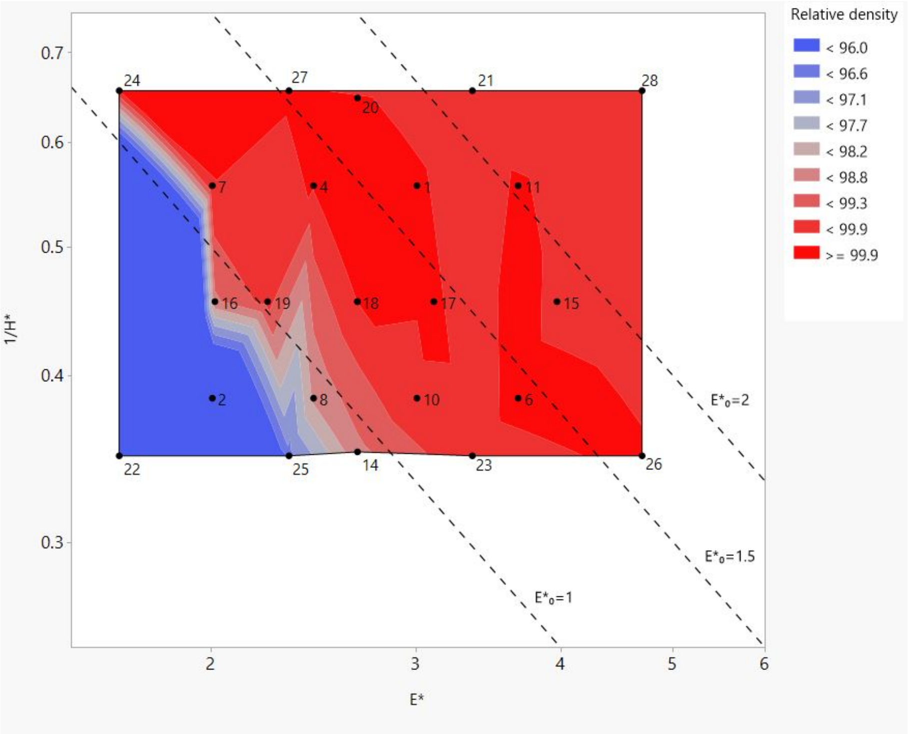

Figure 3.11: Contour plot from JMP software based on dimensionless parameters in T-series

4

Conclusions

This study verifies the fact that densities above 99.9% of IN718 can be achieved when increasing the powder layer thickness of L-PBF process to 80 μm.

The volumetric energy density (VED) and its normalised form as guides for energy input are frequently used by researchers to generalize how the porosity and microstructure are influenced by heat input. This thesis also evaluates how VED and normalised energy density can be correlated with our measurement of relative density and surface roughness. A clear increase of relative density and decrease of side surface roughness were identified with increasing VED. Accordingly, it can be concluded from figures 3.9 and 3.6 that VEDs in the range of 34-50 $[J/mm^3]$ may result in the most optimum combination of relative densities and surface roughness. However, VED does not capture the interaction effects between different parameters (such as between hatch distance and scanning speed) as indicated by the regression analysis. Therefore, suggestions are made for prediction of the final density based on the applied process parameters as shown in regression analysis results. In addition, by translating the applied process parameters into dimensionless parameters, the process map was developed that allows to to predict the final porosity of the component when a different L-PBF machine is used.

This study verifies that the amount of the porosity in the printed sample is dependent on the designed geometry. In addition for higher geometry compliance and therefore less required post processing such as machining, over-melting shall be avoided by keeping the energy input close to the optimum window of key processing parameters.

As a suggestion for future studies, further improvement in the productivity of L-PBF of IN718 is possible by further increasing the layer thickness and accordingly adjusting the key processing parameters. In addition, in order to cross check the accuracy of the results, different methods of characterization such as the Archimedes method for density measurement shall be conducted. Furthermore, more detailed investigations of the product quality such as microstructure and residual stress and testing of mechanical properties are needed to validate the usefulness of IN718 products produced by L-PBF at increased layer thickness.

Bibliography

[1] Conner, B. P., Manogharan, G. P., Martof, A. N., Rodomsky, L. M., Rodomsky, C. M., Jordan, D. C., Limperos, J. W. (2014). Making sense of 3-D printing: Creating a map of additive manufacturing products and services. *Additive Manufacturing, 1-4,* 64–76. http://doi.org/10.1016/j.addma.2014.08.005

[2] Thomas, M., Baxter, G. J., Todd, I. (2016). Normalised model-based processing diagrams for additive layer manufacture of engineering alloys. *Acta Materialia, 108,* 26–35. http://doi.org/10.1016/j.actamat.2016.02.025

[3] Herzog, D., Seyda, V., Wycisk, E., Emmelmann, C. (2016). Additive manufacturing of metals. *Acta Materialia, 117,* 371–392. http://doi.org/10.1016/j.actamat.2016.07.019

[4] Moussaoui, K., Rubio, W., Mousseigne, M., Sultan, T., Rezai, F. (2018). Effects of Selective Laser Melting additive manufacturing parameters of Inconel 718 on porosity, microstructure and mechanical properties. *Materials Science and Engineering: A, 735,* 182–190. http://doi.org/10.1016/j.msea.2018.08.037

[5] Collins, P. C., Haden, C. V., Ghamarian, I., Hayes, B. J., Ales, T., Penso, G., ... Harlow, G. (2014). Progress Toward an Integration of Process–Structure–Property–Performance Models for "Three-Dimensional (3-D) Printing" of Titanium Alloys. *The Minerals, Metals Materials Society 2014, JOM, 66(7).* http://doi.org/https://doi.org/10.1007/s11837-014-1007-y

[6] Tofail, S. A., Koumoulos, E. P., Bandyopadhyay, A., Bose, S., O'Donoghue, L., amp; Charitidis, C. (2018). Additive manufacturing: Scientific and technological challenges, market uptake and opportunities. *Materials Today, 21*(1), 22-37. doi:10.1016/j.mattod.2017.07.001

[7] Frazier, W. E. (2014). Metal Additive Manufacturing: A Review. *Journal of Materials Engineering and Performance, 23*(6), 1917–1928. http://doi.org/10.1007/s11665-014-0958-z

[8] Sames, W. J., List, F. A., Pannala, S., Dehoff, R. R., Babu, S. S. (2016). The metallurgy and processing science of metal additive manufacturing. *International Materials Reviews, 61*(5), 315–360. http://doi.org/10.1080/09506608.2015.1116649

[9] ASTM Standard Guide for Directed Energy Deposition of Metals. http://doi.org/10.1520/f3187-16

[10] Mukherjee, T., Zuback, J.S., De, A. and DebRoy, T. (2016). Printability of alloys for additive manufacturing. *Scientific Reports*, 6(1).

[11] Yadroitsev, I., Krakhmalev, P., Yadroitsava, I. (2015). Hierarchical design principles of selective laser melting for high quality metallic objects. *Additive Manufacturing, 7,* 45–56. http://doi.org/10.1016/j.addma.2014.12.007

[12] Jia, Q., Gu, D. (2014). Selective laser melting additive manufacturing of Inconel 718 superalloy parts: Densification, microstructure and properties. *Journal of Alloys and Compounds, 585,* 713–721. http://doi.org/10.1016/j.jallcom.2013.09.171

[13] Carter, L. N., Attallah, M. M., Reed, R. C. (2012). Laser Powder Bed Fabrication of Nickel-Base Superalloys: Influence of Parameters; Characterisation, Quantification and Mitigation of Cracking. *Superalloys 2012,* 577–586. http://doi.org/10.1002/9781118516430.ch64

[14] Yin, J., Wang, D., Yang, L., Wei, H., Dong, P., Ke, L., Wang, G., Zhu, H. and Zeng, X. (2020). Correlation between forming quality and spatter dynamics in laser powder bed fusion. *Additive Manufacturing*, 31, p.100958.

[15] Babamiri, B.B., Indeck, J., Demeneghi, G., Cuadra, J. and Hazeli, K. (2020). Quantification of porosity and microstructure and their effect on quasi-static and dynamic behavior of additively manufactured Inconel 718. *Additive Manufacturing*, 34, p.101380.

[16] Sola, A., Nouri, A. (2019). Microstructural porosity in additive manufacturing: The formation and detection of pores in metal parts fabricated by powder bed fusion. *Journal of Advanced Manufacturing and Processing, 1*(3). http://doi.org/10.1002/amp2.10021

[17] Hosseini, E., Popovich, V. (2019). A review of mechanical properties of additively manufactured Inconel 718. *Additive Manufacturing, 30*, 100877. http://doi.org/10.1016/j.addma.2019.100877

[18] Spierings, A., Schneider, M., Eggenberger, R. (2011). Comparison of density measurement techniques for additive manufactured metallic parts. *Rapid Prototyping Journal, 17(5),* 380–386. http://doi.org/10.1108/13552541111156504

[19] Hilaire, A., Andrieu, E. and Wu, X. (2019). High-temperature mechanical properties of alloy 718 produced by laser powder bed fusion with different processing parameters. *Additive Manufacturing*, 26, pp.147–160.

[20] Xu, Z., Hyde, C.J., Tuck, C. and Clare, A.T. (2018). Creep behaviour of inconel 718 processed by laser powder bed fusion. *Journal of Materials Processing Technology*, 256, pp.13–24.

[21] Amato, K., Gaytan, S., Murr, L., Martinez, E., Shindo, P., Hernandez, J., Medina, F. (2012). Microstructures and mechanical behavior of Inconel 718 fabricated by selective laser melting. *Acta Materialia, 60(5),* 2229–2239. http://doi.org/10.1016/j.actamat.2011.12.032

[22] Jiang, R., Mostafaei, A., Pauza, J., Kantzos, C. and Rollett, A.D. (2019). Varied heat treatments and properties of laser powder bed printed Inconel 718. *Materials Science and Engineering*: A, 755, pp.170–180.

[23] Ali, U., Fayazfar, H., Ahmed, F. and Toyserkani, E. (2020). Internal surface roughness enhancement of parts made by laser powder-bed fusion additive manufacturing. *Vacuum*, 177, p.109314.

[24] Balachandramurthi, A. R., Moverare, J., Dixit, N., amp; Pederson, R. (2018). Influence of defects and as-built surface roughness on fatigue properties of additively manufactured Alloy 718. *Materials Science and Engineering*: A, 735, 463–474. http://doi.org/10.1016/j.msea.2018.08.072

[25] Khairallah, S., Anderson, A., Rubenchik, A. and King, W., 2016. Laser powder-bed fusion additive manufacturing: Physics of complex melt flow and formation mechanisms of pores, spatter, and denudation zones. *Acta Materialia*, 108, pp.36-45.

[26] Jakumeit, J., Huang, C., Laqua, R., Zielinski, J. and Schleifenbaum, J.H. (2020). Effect of evaporated gas flow on porosity and microstructure of IN718 parts produced by LPBF-processes. *IOP Conference Series: Materials Science and Engineering*, 861, p.012011.

[27] Guo, C., Li, S., Shi, S., Li, X., Hu, X., Zhu, Q. and Ward, R.M. (2020). Effect of processing parameters on surface roughness, porosity and cracking of as-built IN738LC parts fabricated by laser powder bed fusion. *Journal of Materials Processing Technology*, 285, p.116788.

[28] Terris, T. D., Andreau, O., Peyre, P., Adamski, F., Koutiri, I., Gorny, C., Dupuy, C. (2019). Optimization and comparison of porosity rate measurement methods of Selective Laser Melted metallic parts. *Additive Manufacturing, 28* , 802–813. http://doi.org/10.1016/j.addma.2019.05.035

[29] EOS M 290. Retrieved January 28, 2020, from https://www.eos.info/eos-m290

[30] Stegmueller, M.J.R., Grant, R.J. and Schindele, P. (2019). Quantification of the interfacial roughness when coating stainless steel onto aluminium by friction surfacing. *Surface and Coatings Technology,* 375, pp.22–33.

A

Appendix 1

A.1 Detailed result of T-series

Table A.1: Detailed results of T-series; samples T-1 to T-4

Sample	Section	Porosity [%]	RMS (R_q) [µm]	Average RMS [µm]	
				Horizontal plane	Vertical plane
T-1	H-1	0.036	30.5	19.9	24.5
	H-2	0.027	13.8		
	H-3	0.079	14.9		
	H-4	0.024	18.5		
	H-5	0.021	21.8		
	V-1	0.032	41.5		
	V-2	0.017	22.9		
	V-3	0.029	9.1		
T-2	H-1	4.882	97.0	83.5	89.4
	H-2	4.546	19.5		
	H-3	5.708	109.7		
	H-4	5.059	135.0		
	H-5	4.04	56.5		
	V-1	4.148	54.4		
	V-2	5.765	67.0		
	V-3	6.018	146.9		
T-3	H-1	0.079	53.0	37.9	26.6
	H-2	0.082	20.7		
	H-3	0.056	39.7		
	H-4	0.091	50.5		
	H-5	0.048	25.4		
	V-1	0.045	16.2		
	V-2	0.054	26.1		
	V-3	0.077	37.7		
T-4	H-1	0.089	20.5	24.4	31.3
	H-2	0.037	24.7		
	H-3	0.018	31.8		
	H-4	0.039	24.9		
	H-5	0.045	20.2		
	V-1	0.027	46.9		
	V-2	0.028	25.6		
	V-3	0.024	21.3		

Table A.2: Detailed results of T-series; samples T-5 to T-9

Sample	**Section**	**Porosity** [%]	**RMS** (R_q) [µm]	**Average RMS [µm]**	
				Horizontal plane	**Vertical plane**
T-5	H-1	0.039	39.2	33.3	27.8
	H-2	0.242	20.7		
	H-3	0.038	18.0		
	H-4	0.062	34.3		
	H-5	0.079	54.6		
	V-1	0.062	24.0		
	V-2	0.085	28.2		
	V-3	0.057	31.1		
T-6	H-1	0.029	29.5	26.4	26.3
	H-2	0.044	36.1		
	H-3	0.048	23.4		
	H-4	0.064	29.8		
	H-5	0.061	13.2		
	V-1	0.03	34.6		
	V-2	0.024	25.4		
	V-3	0.045	18.8		
T-7	H-1	0.037	47.7	31.1	53.1
	H-2	0.048	34.7		
	H-3	0.076	28.9		
	H-4	0.046	20.0		
	H-5	0.046	24.3		
	V-1	0.06	54.3		
	V-2	0.113	53.5		
	V-3	0.095	51.6		
T-8	H-1	0.393	38.1	50.8	38.6
	H-2	0.761	44.0		
	H-3	0.776	57.8		
	H-4	1.012	92.8		
	H-5	2.066	21.4		
	V-1	1.277	28.5		
	V-2	1.314	35.7		
	V-3	1.312	51.6		
T-9	H-1	0.063	19.9	26.7	24.0
	H-2	0.072	60.0		
	H-3	0.07	15.9		
	H-4	0.07	16.2		
	H-5	0.058	21.3		
	V-1	0.013	19.5		
	V-2	0.027	32.5		
	V-3	0.039	20.1		

Table A.3: Detailed results of T-series; samples T-10 to T-14

Sample	Section	Porosity [%]	RMS (R_q) [µm]	Average RMS [µm] Horizontal plane	Average RMS [µm] Vertical plane
T-10	H-1	0.028	37.3	22.7	24.3
	H-2	0.058	26.2		
	H-3	0.099	17.3		
	H-4	0.082	13.8		
	H-5	0.09	18.8		
	V-1	0.067	35.3		
	V-2	0.131	19.1		
	V-3	0.112	18.6		
T-11	H-1	0.067	30.7	26.3	27.5
	H-2	0.071	16.9		
	H-3	0.018	20.0		
	H-4	0.031	20.5		
	H-5	0.032	43.4		
	V-1	0.03	31.2		
	V-2	0.029	25.5		
	V-3	0.017	25.8		
T-12	H-1	0.058	24.1	28.5	32.3
	H-2	0.076	26.4		
	H-3	0.13	53.9		
	H-4	0.116	16.9		
	H-5	0.144	20.9		
	V-1	0.177	41.3		
	V-2	0.126	34.9		
	V-3	0.098	20.6		
T-13	H-1	0.047	57.8	32.2	53.2
	H-2	0.034	23.8		
	H-3	0.025	19.0		
	H-4	0.022	34.5		
	H-5	0.039	25.8		
	V-1	0.036	69.6		
	V-2	0.026	41.8		
	V-3	0.016	48.3		
T-14	H-1	0.168	21.4	40.6	53.8
	H-2	0.782	70.2		
	H-3	0.737	58.7		
	H-4	0.886	6.9		
	H-5	0.632	45.8		
	V-1	1.405	25.3		
	V-2	1.042	74.8		
	V-3	1.128	61.4		

Table A.4: Detailed results of T-series; samples T-15 to T-19

Sample	**Section**	**Porosity [%]**	**RMS (R_q) [µm]**	**Average RMS [µm]**	
				Horizontal plane	**Vertical plane**
T-15	H-1	0.095	52.2	27.9	22.7
	H-2	0.105	17.7		
	H-3	0.11	15.1		
	H-4	0.108	19.2		
	H-5	0.083	35.2		
	V-1	0.132	37.4		
	V-2	0.057	14.0		
	V-3	0.06	16.8		
T-16	H-1	0.621	50.4	38.1	42.4
	H-2	0.94	25.1		
	H-3	1.217	66.5		
	H-4	0.935	29.0		
	H-5	0.508	19.6		
	V-1	0.778	37.9		
	V-2	1.06	45.4		
	V-3	1.202	43.8		
T-17	H-1	0.052	35.9	32.7	37.9
	H-2	0.055	64.2		
	H-3	0.049	21.6		
	H-4	0.037	11.0		
	H-5	0.031	31.0		
	V-1	0.039	36.9		
	V-2	0.03	48.3		
	V-3	0.034	28.6		
T-18	H-1	0.01	34.7	31.6	37.4
	H-2	0.024	35.1		
	H-3	0.017	19.1		
	H-4	0.034	33.1		
	H-5	0.033	36.1		
	V-1	0.01	43.8		
	V-2	0.067	29.1		
	V-3	0.056	39.3		
T-19	H-1	0.189	26.4	26.5	29.3
	H-2	0.153	31.8		
	H-3	0.148	43.7		
	H-4	0.336	13.6		
	H-5	0.605	17.2		
	V-1	0.369	20.1		
	V-2	0.245	49.4		
	V-3	0.35	18.4		

Table A.5: Detailed results of T-series; samples T-20 to T-24

Sample	Section	Porosity [%]	RMS (R_q) [µm]	Average RMS [µm]	
				Horizontal plane	Vertical plane
T-20	H-1	0.183	15.3	20.0	26.5
	H-2	0.018	32.8		
	H-3	0.021	15.1		
	H-4	0.034	22.3		
	H-5	0.021	14.3		
	V-1	0.048	24.0		
	V-2	0.027	21.9		
	V-3	0.029	33.6		
T-21	H-1	0.55	28.3	26.6	48.2
	H-2	0.221	32.4		
	H-3	0.181	14.4		
	H-4	0.117	34.1		
	H-5	0.297	23.7		
	V-1	0.37	39.4		
	V-2	0.213	67.5		
	V-3	0.131	37.7		
T-22	H-1	17.148	106.6	114.9	104.7
	H-2	26.16	109.6		
	H-3	15.007	150.7		
	H-4	18.299	110.2		
	H-5	19.073	97.4		
	V-1	17.399	77.2		
	V-2	19.451	127.2		
	V-3	18.437	109.6		
T-23	H-1	0.092	82.2	31.2	50.9
	H-2	0.066	13.8		
	H-3	0.092	3.8		
	H-4	0.087	10.7		
	H-5	0.102	45.5		
	V-1	0.112	58.7		
	V-2	0.133	30.6		
	V-3	0.148	63.3		
T-24	H-1	0.031	6.7	30.8	26.3
	H-2	0.117	41.2		
	H-3	0.099	23.0		
	H-4	0.047	53.3		
	H-5	0.131	30.1		
	V-1	0.048	28.5		
	V-2	0.057	30.7		
	V-3	0.035	19.7		

Table A.6: Detailed results of T-series; samples T-25 to T-28

Sample	Section	Porosity [%]	RMS (R_q) [µm]	Average RMS [µm]	
				Horizontal plane	Vertical plane
T-25	H-1	3.156	58.7	51.9	55.0
	H-2	1.846	7.3		
	H-3	1.583	30.1		
	H-4	2.301	66.7		
	H-5	3.516	96.5		
	V-1	2.405	38.5		
	V-2	2.513	64.4		
	V-3	2.982	62.0		
T-26	H-1	0.062	32.3	42.3	28.4
	H-2	0.04	48.7		
	H-3	0.027	27.4		
	H-4	0.043	45.6		
	H-5	0.059	57.4		
	V-1	0.058	33.6		
	V-2	0.037	18.1		
	V-3	0.04	33.6		
T-27	H-1	0.051	28.3	28.4	46.0
	H-2	0.032	27.9		
	H-3	0.046	21.5		
	H-4	0.024	19.3		
	H-5	0.025	44.9		
	V-1	0.023	71.4		
	V-2	0.032	32.9		
	V-3	0.033	33.6		
T-28	H-1	0.829	18.0	22.3	38.7
	H-2	0.538	15.8		
	H-3	0.26	14.6		
	H-4	0.233	27.5		
	H-5	0.419	35.6		
	V-1	0.997	33.9		
	V-2	0.327	26.1		
	V-3	0.124	56.1		

A.2 R-studio

A.2.1 C-series

```
> str(C_series)
'data.frame': 20 obs. of  4 variables:
 $ P: num  -1 -1 0 1 0 1 -1 1 0 -1 ...
 $ S: num  -1 1 0 1 0 -1 1 1 0 -1 ...
 $ H: num  -1 1 0 -1 0 1 -1 1 0 1 ...
 $ D: num  100 95.4 99.9 100 99.9 ...
> summary(C_series)
       P                S                H                D
 Min.   :-1.63   Min.   :-1.63   Min.   :-1.63   Min.   :95.38
 1st Qu.:-0.25   1st Qu.:-0.25   1st Qu.:-0.25   1st Qu.:99.91
 Median : 0.00   Median : 0.00   Median : 0.00   Median :99.94
 Mean   : 0.00   Mean   : 0.00   Mean   : 0.00   Mean   :99.50
 3rd Qu.: 0.25   3rd Qu.: 0.25   3rd Qu.: 0.25   3rd Qu.:99.95
 Max.   : 1.63   Max.   : 1.63   Max.   : 1.63   Max.   :99.98
> print(C_series)
       P     S     H      D
1  -1.00 -1.00 -1.00 99.960
2  -1.00  1.00  1.00 95.380
3   0.00  0.00  0.00 99.943
4   1.00  1.00 -1.00 99.954
5   0.00  0.00  0.00 99.948
6   1.00 -1.00  1.00 99.936
7  -1.00  1.00 -1.00 99.956
8   1.00  1.00  1.00 96.896
9   0.00  0.00  0.00 99.941
10 -1.00 -1.00  1.00 99.934
11  1.00 -1.00 -1.00 99.947
12  0.00  0.00  0.00 99.941
13  0.00  0.00  0.00 99.948
14  0.00  0.00  1.63 99.181
15  0.00 -1.63  0.00 99.932
16  0.00  1.63  0.00 99.479
17  1.63  0.00  0.00 99.979
18  0.00  0.00  0.00 99.947
19 -1.63  0.00  0.00 99.846
20  0.00  0.00 -1.63 99.963
>
>
> C_Model <- lm(D ~ P*S + P*H + H*S +I(P^2)+I(S^2)+ I(H^2),C_series)
> summary(C_Model)

Call:
lm(formula = D ~ P * S + P * H + H * S + I(P^2) + I(S^2) + I(H^2),
    data = C_series)
```

```
Residuals:
     Min       1Q   Median       3Q      Max
-1.11648 -0.32308 -0.04738  0.13970  1.18422

Coefficients:
            Estimate Std. Error t value Pr(>|t|)
(Intercept)  99.9894     0.3033 329.664  < 2e-16 ***
P             0.1292     0.2045   0.632  0.54169
S            -0.6256     0.2045  -3.060  0.01204 *
H            -0.6719     0.2045  -3.286  0.00820 **
I(P^2)       -0.1761     0.2058  -0.855  0.41232
I(S^2)       -0.2540     0.2058  -1.234  0.24543
I(H^2)       -0.3042     0.2058  -1.478  0.17018
P:S           0.1906     0.2638   0.723  0.48640
P:H           0.1916     0.2638   0.727  0.48417
S:H          -0.9496     0.2638  -3.600  0.00484 **
---
Signif. codes:  0 ‘***’ 0.001 ‘**’ 0.01 ‘*’ 0.05 ‘.’ 0.1 ‘ ’ 1

Residual standard error: 0.746 on 10 degrees of freedom
Multiple R-squared:  0.7939,Adjusted R-squared:  0.6083
F-statistic: 4.279 on 9 and 10 DF,  p-value: 0.01654
```

A.2.2 T-series

```
> str(T_series)
'data.frame': 28 obs. of  4 variables:
 $ P: num  -1 -1 0 1 0 1 -1 1 0 -1 ...
 $ S: num  -1 1 0 1 0 -1 1 1 0 -1 ...
 $ H: num  -1 1 0 -1 0 1 -1 1 0 1 ...
 $ D: num  100 92.8 99.9 99.9 99.9 ...
> summary(T_series)
       P                S                H                D
 Min.   :-1.67   Min.   :-1.68   Min.   :-1.68   Min.   :73.43
 1st Qu.:-1.00   1st Qu.:-1.00   1st Qu.:-1.00   1st Qu.:99.51
 Median : 0.00   Median : 0.00   Median : 0.00   Median :99.89
 Mean   : 0.00   Mean   : 0.00   Mean   : 0.00   Mean   :98.40
 3rd Qu.: 1.00   3rd Qu.: 1.00   3rd Qu.: 1.00   3rd Qu.:99.94
 Max.   : 1.67   Max.   : 1.68   Max.   : 1.68   Max.   :99.96
> print(T_series)
      P     S     H        D
1  -1.00 -1.00 -1.00 99.95445
2  -1.00  1.00  1.00 92.81021
3   0.00  0.00  0.00 99.90774
4   1.00  1.00 -1.00 99.94734
5   0.00  0.00  0.00 99.88560
6   1.00 -1.00  1.00 99.94076
7  -1.00  1.00 -1.00 99.89733
8   1.00  1.00  1.00 98.35811
```

```
9   0.00  0.00  0.00 99.92838
10 -1.00 -1.00  1.00 99.87440
11  1.00 -1.00 -1.00 99.94940
12  0.00  0.00  0.00 99.83015
13  0.00  0.00  0.00 99.95767
14  0.00  0.00  1.63 98.64687
15  0.00 -1.63  0.00 99.86989
16  0.00  1.63  0.00 98.68109
17  1.63  0.00  0.00 99.94356
18  0.00  0.00  0.00 99.94978
19 -1.63  0.00  0.00 99.56969
20  0.00  0.00 -1.63 99.93465
21 -1.67 -1.68 -1.68 99.63767
22 -1.67  1.68  1.68 73.43182
23 -1.67 -1.68  1.68 99.84230
24 -1.67  1.68 -1.68 99.90303
25  1.67  1.68  1.68 96.38243
26  1.67 -1.68  1.68 99.93551
27  1.67  1.68 -1.68 99.95387
28  1.67 -1.68 -1.68 99.33613
>
>
> T_Model <- lm(D ~ P*S + P*H + H*S+I(P^2)+I(S^2)+ I(H^2),T_series)
> summary(T_Model)

Call:
lm(formula = D ~ P * S + P * H + H * S + I(P^2) + I(S^2) + I(H^2),
    data = T_series)

Residuals:
    Min      1Q  Median      3Q     Max
-5.7122 -1.4858 -0.3199  1.8923  4.8506

Coefficients:
            Estimate Std. Error t value Pr(>|t|)
(Intercept) 100.2589     0.7731 129.690  < 2e-16 ***
P             1.2444     0.4319   2.882  0.00993 **
S            -1.6577     0.4302  -3.853  0.00117 **
H            -1.6712     0.4302  -3.884  0.00109 **
I(P^2)       -0.3634     0.5840  -0.622  0.54160
I(S^2)       -0.5468     0.5803  -0.942  0.35857
I(H^2)       -0.5410     0.5803  -0.932  0.36353
P:S           0.9955     0.3060   3.254  0.00441 **
P:H           0.9993     0.3060   3.266  0.00429 **
S:H          -1.3335     0.3043  -4.382  0.00036 ***
---
Signif. codes:  0 ‘***’ 0.001 ‘**’ 0.01 ‘*’ 0.05 ‘.’ 0.1 ‘ ’ 1

Residual standard error: 2.578 on 18 degrees of freedom
```

```
Multiple R-squared:  0.8307,Adjusted R-squared:  0.746
F-statistic: 9.813 on 9 and 18 DF,  p-value: 2.601e-05
```

A.3 Dimensionless energy per unite volume

Table A.7: Dimensionless parameters based on in equations 1.2-1.4 for C-series

Sample name	**E***	**1/H***	**Relative density [%]**
C-1	3.0106	0.5556	99.960
C-2	2.0071	0.3846	95.380
C-3	2.6761	0.4545	99.943
C-4	2.4531	0.5556	99.954
C-5	2.6761	0.4545	99.948
C-6	3.6796	0.3846	99.936
C-7	2.0071	0.5556	99.956
C-8	2.4531	0.3846	96.896
C-9	2.6761	0.4545	99.941
C-10	3.0106	0.3846	99.934
C-11	3.6796	0.5556	99.947
C-12	2.6761	0.4545	99.941
C-13	2.6761	0.4545	99.948
C-14	2.6761	0.3505	99.181
C-15	3.9740	0.4545	99.932
C-16	2.0172	0.4545	99.479
C-17	3.1131	0.4545	99.979
C-18	2.6761	0.4545	99.947
C-19	2.2391	0.4545	99.846
C-20	2.6761	0.6465	99.963

Table A.8: Dimensionless parameters based on in equations 1.2-1.4 for T-series

Sample name	**E***	**1/H***	**Relative density [%]**
T-1	3.0106	0.5556	99.954
T-2	2.0071	0.3846	92.810
T-3	2.6761	0.4545	99.908
T-4	2.4531	0.5556	99.947
T-5	2.6761	0.4545	99.886
T-6	3.6796	0.3846	99.941
T-7	2.0071	0.5556	99.897
T-8	2.4531	0.3846	98.358
T-9	2.6761	0.4545	99.928
T-10	3.0106	0.3846	99.874
T-11	3.6796	0.5556	99.949
T-12	2.6761	0.4545	99.830
T-13	2.6761	0.4545	99.958
T-14	2.6761	0.3505	98.647
T-15	3.9740	0.4545	99.870
T-16	2.0172	0.4545	98.681
T-17	3.1131	0.4545	99.944
T-18	2.6761	0.4545	99.950
T-19	2.2391	0.4545	99.570
T-20	2.6761	0.6465	99.935
T-21	3.3603	0.6548	99.638
T-22	1.6688	0.3481	73.432
T-23	3.3603	0.3481	99.842
T-24	1.6688	0.6548	99.903
T-25	2.3363	0.3481	96.382
T-26	4.7045	0.3481	99.936
T-27	2.3363	0.6548	99.954
T-28	4.7045	0.6548	99.336